

Observational Signatures of Supermassive Black Hole Binaries

DANIEL J. D’ORAZIO¹ AND MARIA CHARISI²

¹*Niels Bohr International Academy, Niels Bohr Institute, Blegdamsvej 17, 2100 Copenhagen, Denmark*

²*Department of Physics & Astronomy, Vanderbilt University, 2301 Vanderbilt Place, Nashville, TN 37235, USA*

ABSTRACT

Despite solid theoretical and observational grounds for the pairing of supermassive black holes (SMBHs) after galaxy mergers, definitive evidence for the existence of close (sub-parsec) separation SMBH binaries (SMBHBs) approaching merger is yet to be found. This chapter reviews techniques aimed at discovering such SMBHBs in galactic nuclei. We motivate the search with a brief overview of SMBHB formation and evolution, and the gaps in our present-day theoretical understanding. We then present existing observational evidence for SMBHBs and discuss ongoing efforts to provide definitive evidence for a population at sub-parsec orbital separations, where many of the aforementioned theoretical gaps lie. We conclude with future prospects for discovery with electromagnetic (primarily time-domain) surveys, high-resolution imaging experiments, and low-frequency gravitational-wave detectors.

1. INTRODUCTION

In the 1960’s the discovery of quasars as extra-galactic entities (Schmidt 1963) and identification of their power source with accreting supermassive black holes (SMBHs; Robinson et al. 1965; Lynden-Bell 1969) led towards the modern picture of SMBHs occupying the centers of nearly all massive galaxies (Kormendy & Richstone 1995). Soon after these first identifications of SMBHs as quasar power sources, Thorne & Braginskii (1976) demonstrated that the initial collapse or mergers of SMBHs would generate bursts of gravitational radiation detectable at Earth. Begelman et al. (1980) carried this further by painting a first picture of the relevant astrophysical processes that could bring two single SMBHs together after collisions of galaxies. They additionally posited multiple signatures that would provide evidence for SMBH binaries (SMBHBs) and their pairings in galactic nuclei. They argued that the binary hardening process could create observable light deficits in the cores of galaxies, and that the orbital motion of SMBH pairs could generate peculiar radio jet morphology, emission line offsets, or photometric variability (see also Komberg 1968).

In the forty years since the seminal work by Begelman et al. (1980), the modeling of environmental interactions that do, or do not bring SMBHs towards merger is still an active topic at the heart of a major open problem in astrophysics: the final-parsec problem (§2; Milosavljević & Merritt 2003; Merritt & Milosavljević 2005; Colpi 2014). While theoretical work has since developed solutions to the initial posing of the final parsec problem, *i.e.*, identifying processes which will bring two SMBHs close enough to merge in a Hubble time (see, *e.g.*, §2), the mystery of which processes operate in nature remains. In essence, this problem is similar to the current investigation of astrophysical formation channels of the stellar mass black hole binaries detected in gravitational waves (GWs) by LIGO-Virgo-KAGRA: there exist formation channels which could work in theory, but which of these operate in nature, and in what proportion is still unknown (*e.g.*, Zevin et al. 2021). For the SMBHBs, a concise, modern statement of the final parsec problem, or what we might now call the *supermassive-merger problem*, is *galaxies containing SMBHs merge, but do their SMBHBs also merge, and how?*

Further modeling of SMBHB environmental interactions is needed for reliable population predictions. But importantly, discovery of members of the population at different stages of the SMBHB lifespan is needed to test and hone the understanding of astrophysics that goes into these predictions. This review focuses on the latter, with a brief introduction to the former. We focus primarily on electromagnetic discovery for a few reasons:

1. While GW observations of SMBHB inspiral and merger will give definitive evidence for the population at its end stages, electromagnetic identification offers a demographic probe at earlier stages that is critical for understanding the supermassive-merger problem, and the whole lifespan of the SMBHB (see Figure 1).
2. Electromagnetic identification methods are varied and evolving, and it is unclear which (combination of) methods are the most promising for providing definitive evidence for SMBHBs. Hence, we attempt to make clear the ideas behind the different methods and give the pros and cons of each throughout.
3. We are entering an era where unprecedented quantities of electromagnetic data will soon be available via photometric and spectroscopic surveys, *e.g.*, the Vera Rubin Observatory’s Legacy Survey of Space and Time (LSST, [Ivezić et al. 2019](#)) and SDSS-V ([Kollmeier et al. 2017](#)), and surveys with the planned Roman Space Telescope ([Wang et al. 2022b](#)); as well as high resolution radio and optical telescopes, *e.g.*, the Next Generation Very Large Array (ngVLA, [Burke-Spolaor et al. 2018](#)), the Event Horizon Telescope (EHT, [Event Horizon Telescope Collaboration et al. 2019](#)) and its extensions (*e.g.*, ngEHT, EHE, [Lico et al. 2023](#); [Kurczynski et al. 2022](#)), and GRAVITY+ ([Gravity+ Collaboration et al. 2022](#)). These, along with the James Webb Space Telescope (JWST, [Gardner et al. 2006](#)), and planned or proposed missions at multiple wavelengths, *e.g.*, the ATHENA X-ray mission ([Nandra et al. 2013](#); [Marchesi et al. 2020](#)) will provide new observational handles on the SMBHBs and guide methods for discovery.

In §2, we briefly review the physical processes thought to bring SMBHBs together and provide some basic expectations for the SMBHB population. These expectations motivate where and how to look for SMBHBs at close separation, which we discuss in the opening of §3. The remainder of §3 details SMBHB identification methods, quintessential candidates, if any, and the pros and cons of each method. We discuss future prospects for observational identification of SMBHBs in §4. A non-complete, but extensive list of SMBHB candidates is compiled at the end of the chapter, in §5. We have not aimed for completeness in this review, but rather, have given a broad overview and introduction to promising detection methods while providing further focus on a few of the most exciting topics for us at this time. For other recent and related reviews see [Burke-Spolaor et al. \(2018\)](#); [Wang & Li \(2020\)](#); [Bogdanović et al. \(2022\)](#) and §2 of [Amaro-Seoane et al. \(2023\)](#).

2. A BRIEF PRIMER ON THE SMBHB LIFESPAN

To find something, you need to know where to look and what to look for. To gain insight we first review the SMBHB lifespan: the physical components as well as temporal and spatial scales associated with bringing two SMBHBs together from galactic merger to the final SMBHB coalescence. A more in-depth look at these processes is provided in Chapter 3 of this book.

2.1. Overview

For our purposes, the SMBHB merger process can be described by an initial condition and three steps, which qualitatively resemble the picture put forward by [Begelman et al. \(1980\)](#).

Initial Condition—The SMBH occupation fraction and galaxy merger rate at a given redshift provide the initial pairings of SMBHBs at that redshift that may eventually form tight binaries at lower redshifts. While we have observational constraints from galaxy merger rates and the occurrence rates of dual active galactic nuclei (AGN, see §3.2.1), it is still a challenge to quantify the SMBHB pairing rate and distribution across redshift (*e.g.*, [Koss et al. 2019](#), and references therein).

Large-Scale Evolution—The SMBHBs delivered through galactic merger sink to the center of the newly formed galaxy via dynamical friction. After of order a galactic dynamical time ($\sim 10^8$ yr), the two become bound relative to the surrounding stellar cluster, forming an SMBHB at $\mathcal{O}(1 - 10)$ pc separations. This limit is denoted by the dot-dashed grey line in Figure 1 indicating where the binary orbital velocity is of order the surrounding velocity dispersion of stars (the so-called “hard-binary” limit [Begelman et al. 1980](#); [Milosavljević & Merritt 2003](#)). Uncertainties in the efficacy of dynamical friction leading to binary formation at \sim kpc scales also hinder our current theoretical grasp on the SMBHB population (*e.g.*, see §2 of [Amaro-Seoane et al. 2023](#), and references therein), but we do not focus on them here.

Small Scale Evolution—Gravitational radiation carries away energy and angular momentum from the binary which decreases its semi-major axis and circularizes the orbit. A criterion for where GWs become important for binary evolution can be estimated to be where the binary lifetime due to gravitational radiation becomes shorter than the age of the universe. This happens when the

separation, a_{GW} , and the orbital period, P_{GW} of the binary are given by

$$\begin{aligned} a_{\text{GW}} &\approx 0.049 \text{ pc} \left(\frac{q/(1+q)^2}{0.25} \right)^{1/4} \left(\frac{T}{1.3 \times 10^{10} \text{ yr}} \right)^{1/4} \left(\frac{M}{10^8 M_{\odot}} \right)^{3/4} \\ P_{\text{GW}} &\approx 100.5 \text{ yr} \left(\frac{q/(1+q)^2}{0.25} \right)^{3/8} \left(\frac{T}{1.3 \times 10^{10} \text{ yr}} \right)^{3/8} \left(\frac{M}{10^8 M_{\odot}} \right)^{5/8}, \end{aligned} \quad (1)$$

where $q = M_2/M_1 \leq 1$ is the mass ratio of the binary with total mass $M = M_1 + M_2$ and T is the GW-driven merger time. Only binaries with orbital separations smaller (or periods shorter) than this can be driven to merger by GWs alone. There are other meaningful criteria for when binary evolution becomes dominated by GWs, but the above equations provide a useful reference which is agnostic of other processes operating near merger, *e.g.*, gas decoupling (Haiman et al. 2009). The steep dependence of the GW-driven merger time T on the orbital separation a (i.e. $T \propto a^4$) is in part responsible for the difficulty in driving the SMBHB through intermediate scale separations and the “final parsec” of its evolution discussed next.

Intermediate Scale Evolution (sub-parsec)—At small enough binary separations, dynamical friction becomes inefficient, and binary evolution is driven by interactions with its immediate environment (*e.g.*, stars). However, the number of stars on centrophilic orbits, which can remove energy and angular momentum from the binary, is quickly depleted. Initial treatments of the problem found that, if the binary interacts only with a spherical distribution of surrounding stars, the binary stalls in the final parsec before merger (Milosavljević & Merritt 2003). This uncertainty in how SMBHBs might cross the final parsec on the path towards GW-driven merger is often referred to as the “final-parsec problem,” as discussed in the introduction to this Chapter and explored further in Chapter 3 of this book.

Currently, there is no firm evidence against the stalling of all SMBHBs, although this may soon change if the recently detected evidence for a GW background can be definitively tied, at least in part, to a population of inspiralling SMBHBs (see §3.7). In addition, there are multiple, realistic astrophysical processes that could allow the binary to breach the final parsec:

- **Stars** in non-spherical distributions can torque the orbits of individual stars to lower-angular momentum orbits that interact with the binary. Triaxial stellar distributions have been shown to be capable of such “loss-cone”¹ refilling at a high enough rate to merge the binary in a Hubble time (Yu 2002; Merritt & Poon 2004; Khan et al. 2011; Preto et al. 2011).
- **Gas** can be torqued to the centers of galaxies following galactic merger (*e.g.*, Barnes & Hernquist 1996; Barnes 2002) and could facilitate binary merger by removing energy and angular momentum from the binary orbit.
- **Other** processes/mechanisms can also push the binary to small separations. Interaction of the binary with an incoming massive perturber (*e.g.*, Perets et al. 2007) or star cluster (*e.g.*, Bortolas et al. 2018) may facilitate merger, or the interaction of the nuclear star clusters surrounding each SMBH may be important for deciding the fate of the SMBH pair (*e.g.*, Ogiya et al. 2020). Even if all other processes fail, a subsequent galaxy merger could introduce a third black hole (*e.g.*, Ryu et al. 2018; Bonetti et al. 2019).

So the final-parsec problem as originally posed is no longer a problem. However, the question of how SMBHBs do or do not come together, the *supermassive merger problem* is still very much open. It is not a problem in devising methods for how to get SMBHBs to merge, but rather in understanding how it is done in nature: how do SMBHBs interact with their astrophysical environments and do, or do not come together. A solution to the *supermassive merger problem* requires further modeling of SMBHB-environmental interactions, and, perhaps more importantly, it requires definitive evidence for or against SMBHBs in the intermediate, sub-parsec stages of evolution. How to find such evidence is the topic of this review.

2.2. Connection to Population Predictions

To establish the connection between the above physical processes describing binary formation and evolution and the expectations for a discoverable SMBHB population, we briefly present a mathematical model describing the population and its evolution. We write a continuity equation describing the evolution in time (and thus in redshift) of the number of SMBHBs per orbital parameters. For demonstration, we write the SMBHB number density \mathcal{D} per orbital frequency f and total binary mass M , as a function of time t , i.e. $\mathcal{D}(f, M, t)$, valid from the formation of a bound binary down to merger,

$$\partial_t \mathcal{D} + \partial_f (\dot{f} \mathcal{D}) + \partial_M (\dot{M} \mathcal{D}) = \mathcal{S}, \quad \mathcal{D} \equiv \frac{d^2 n}{df dM}, \quad (2)$$

¹ Referring to the shape of orbital energy and angular momentum space that results in strong interactions with the binary.

where \dot{f} and \dot{M} are rates-of-change of the binary orbital frequency and total binary mass, which generally depend on time and orbital parameters, and \mathcal{S} describes the rate at which new hard binaries are formed. One can solve this equation with the desired complexity in choices of initial redshift distribution, black hole growth, and orbital evolution. The result is a prediction for the population, \mathcal{D} .

We derive a relatively simple population model by linking the EM-bright SMBHB population to the quasar population following [Soyuer et al. \(2021\)](#) and relying on similar, previous approaches ([Sesana et al. 2005](#); [Christian & Loeb 2017](#)). We assume:

- A constant fraction η_{bin} of all quasars are triggered by a galaxy merger that eventually results in the formation and merger of an SMBHB over the course of the quasar lifetime t_Q .
- The quasar redshift and mass distribution traces the SMBHB merger and total binary mass distribution. Then the differential volumetric merger rate is

$$\frac{d\mathcal{R}}{dM} = \frac{\eta_{\text{bin}}}{\tau_Q} \frac{d^2 N_Q}{dLdV} \frac{dL}{dM} \quad (3)$$

where $d^2 N_Q/(dLdV)$ is an observationally determined quasar luminosity function, and we relate the quasar bolometric luminosity L to the binary mass M by choosing a distribution of accretion rates normalized in terms of the Eddington rate (*e.g.*, [Shankar et al. 2013](#)).

- The population is in steady state, consists only of circular orbits, and because we tie the binary mass to the quasar central mass, we do not include mass growth ($\dot{M} = 0$). Then at scales below where the source term contributes², Eq. (2) has solution $\dot{f}\mathcal{D} = \text{const.} = d\mathcal{R}/dM$.

With these simplifying assumptions, we can write the solution for the binary number density as

$$n_{\text{bin}} = \int \frac{d\mathcal{R}}{dM} \frac{df}{\dot{f}} dM, \quad (4)$$

where $d\mathcal{R}/dM$ is the volumetric merger rate per total binary mass for a specified population, and where we have further assumed that binary mass ratios are fixed over the observation time.

Then the total number of quasars within redshift z , total mass less than M , and orbital frequency above f is

$$N_{\text{bin}}(> f) = 4\pi \frac{\eta_{\text{bin}}}{t_Q} \int_0^z \int_0^M \int_f^{f_{\text{ISCO}}} \frac{dV}{dz} \frac{d^2 N_Q}{dLdV} \frac{dL}{dM} \frac{f}{\dot{f}} d\log f dM dz, \quad (5)$$

where dV/dz is the angle integrated cosmological volume element in a flat universe ([Hogg 1999](#)). The integration must be limited to the range of applicability of the quasar luminosity function (*e.g.*, a luminosity cut).

It is useful to divide by the total number of quasars in the same domain to estimate the fraction of AGN that harbour SMBHBs in the given mass, frequency and redshift range. This gives,

$$\frac{N_{\text{bin}}(> f)}{N_Q} \approx \eta_{\text{bin}} \frac{\langle t_{\text{res}} \rangle}{t_Q}, \quad (6)$$

where $t_{\text{res}} \equiv f/\dot{f}$ is the binary orbital parameter-dependent residence time (*i.e.* the time that the binary spends at a given orbital period), and the angle brackets denote a weighted average over the quasar mass and redshift distribution. This says that the longer the binary residence time, the higher the fraction of AGN that host SMBHBs with orbital frequency greater than f , and so the more abundant they should be in a survey of quasars. Note that this argument holds even if AGN activity is intermittent ([Goulding et al. 2018](#)) over the binary lifetime, as long as the AGN has active stages that last for $\gtrsim t_{\text{res}}$ when the binary is at orbital frequency f (see also [Haiman et al. 2009](#)); and the residence time $\sim 10^5 \text{ yr} (f^{-1}/5.1 \text{ yr})^{8/3} (M/10^8 M_\odot)^{-5/3}$ can be short compared to expected AGN lifetimes $\sim 10^7 - 10^8 \text{ yr}$ ([Martini 2004](#); [Goulding et al. 2018](#)). That the binary is bright during these times is of course an assumption of the model and subsumed into η_{bin} . For application to observations, one must also apply a flux limit which restricts the accessible luminosity and redshift space.

² The source function does not affect the solution for binaries at separations closer than a minimum separation scale at birth (*e.g.*, [Christian & Loeb 2017](#)). If however we can probe the population on such a scale, *e.g.*, with observations of parsec-scale binaries and their progenitors such as dual AGN (§3.2), then we may also access this birth term.

This approach has been used in a number of works to estimate properties of the SMBHB population (*e.g.*, Haiman et al. 2009; D’Orazio & Loeb 2019; Xin & Haiman 2021; Casey-Clyde et al. 2022). Further complexifications allow different orbital parameters to evolve, include other hardening mechanisms such as interactions with gas and stars (*e.g.*, Mingarelli et al. 2017; D’Orazio & Loeb 2018; Bortolas et al. 2021), include non-trivial source functions, or rather than anchor to an observed quasar luminosity function, simulate the entire process with sub-grid prescriptions for SMBHB evolution painted onto the outputs of cosmological simulations (*e.g.*, Kelley et al. 2017a,b, 2019b, 2021).

3. OBSERVATIONAL SEARCH METHODS

In the previous section we discussed how to use models of binary orbital evolution (\dot{f}, \dot{M}, \dots) to predict populations ($\mathcal{D} \equiv \partial^2 n / \partial f \partial M$). To envision the role of observations, consider an opposite approach to Eq. (2), where we sample \mathcal{D} through observations of SMBHBs at different stages of their lives, and thus constrain \dot{f} and \dot{M} , allowing us to constrain the physics of SMBHB orbital decay and growth. We are not aware of a theoretical study determining the sufficient or optimal sampling of \mathcal{D} through observations of SMBHB candidates to make non-trivial conclusions about \dot{f} , \dot{M} , or other orbital change rates. However, multiple studies have applied candidate demographics towards gaining insight into underlying orbital decay mechanisms (*e.g.*, D’Orazio et al. 2015a; Charisi et al. 2016; Goulding et al. 2019), though with the caveat that the population does not consist of confirmed SMBHBs, or consists of a few (or even one) systems. Hence, we now review the existing evidence for, and various techniques to find, SMBHBs from the largest scales, down to the smallest. Figure 1 serves as an overview of the methods and candidates that we review in this Section.

3.1. How and Where to Look: Population Expectations

The idea that SMBHBs exist in galactic nuclei and ideas for finding them have been around for over 40 years (Begelman et al. 1980). So why do we still have only circumstantial evidence for their existence at sub-parsec scales, and what would constitute definitive evidence?

Where to look? To find electromagnetic evidence, an SMBHB must be electromagnetically bright. In the majority of cases, this suggests that we should target a special type of galactic nuclei, namely active galactic nuclei (AGN)³, in which one of both SMBH(s) is(are) accreting (see, however, § 3.2.2 for binary tidal disruptions in §3.4.1, which do not require an AGN). So our search will be guided by the distribution of AGN and the fraction which harbor an SMBHB in a range of orbital separations for which a specific observational strategy is sensitive (see Figure 1). An estimate for this fraction will also guide searches. In §2.2 we presented a model useful for estimating this in terms of binary residence time and the quasar lifetime (*i.e.*, length of time for which the AGN is active). If we assume decay of circular orbits due to GW emission and make a point evaluation (simply for illustrative purposes here) to remove the average over the quasar luminosity function in Eq. (5), then we can estimate the fraction of quasars containing SMBHBs with orbital periods shorter than a fixed period $P \equiv f^{-1}$, as,

$$\frac{N_{\text{bin}}}{N_Q} \approx 10^{-3} \eta_{\text{bin}} \frac{(1+q)^2}{4q} \left(\frac{P}{5.1 \text{ yr}} \right)^{8/3} \left(\frac{M}{10^9 M_\odot} \right)^{-5/3} \left(\frac{t_Q}{10^8 \text{ yr}} \right)^{-1}, \quad (7)$$

or equivalently

$$\frac{N_{\text{bin}}}{N_Q} \approx 10^{-3} \eta_{\text{bin}} \frac{(1+q)^2}{4q} \left(\frac{P}{5.1 \text{ yr}} \right) \left(\frac{N_a}{150} \right)^{5/2} \left(\frac{t_Q}{10^8 \text{ yr}} \right)^{-1}, \quad (8)$$

where $N_a \equiv a/(2GM/c^2)$ is the separation expressed in Schwarzschild radii, q , and M are the binary mass ratio and total mass, respectively (see also Haiman et al. 2009, this is the same as their Eq. (50) if $\eta_{\text{bin}} = 1$). The choice of orbital periods of $\mathcal{O}(\text{yr})$ is appropriate for the baselines of modern time-domain surveys. For reference, a binary with total mass $10^9 M_\odot$ and a 5.1 yr orbital period has a separation of 0.014 pc.

Hence, to obtain a sample of 100 SMBHBs, our simple model predicts that one must survey $\gtrsim 10^5 / \eta_{\text{bin}}$ quasars. If the aim is to capture orbital variations (*e.g.*, §3.3 or §3.4 below), then any observing program that can survey the required number of quasars must also operate for at least one orbital period, but likely more in order to build the signal significance. Adopting the quasar luminosity function from Hopkins et al. (2007)⁴, we find that the number of AGN/quasars between bolometric luminosities of $10^{42} - 10^{48.5} \text{ erg/s}$ does not rise above 10^5 (10^6) until $z \sim 0.05$ ($z \sim 0.1$). This suggests that a full sky survey of quasars must monitor beyond $z \sim 0.1$, for a decade ($\sim 2P$).

³ Note that throughout the paper we use the terms AGN and quasar interchangeably – quasars are a sub-class of AGN characterized by their high luminosity.

⁴ The pure-luminosity-evolution, double-power-law with redshift dependent slopes. See the last row of Table 3 labeled “Full.”

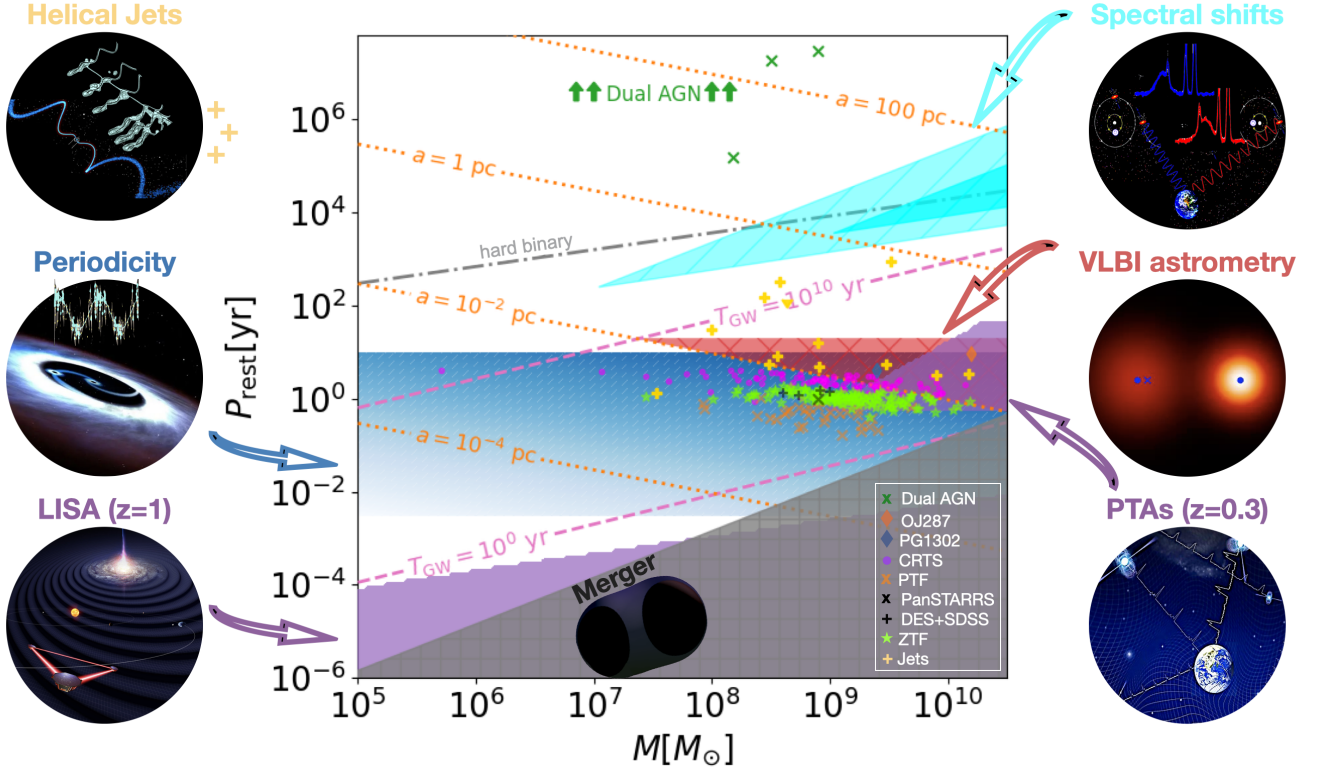


Figure 1. A visual guide to the Chapter: Observational signatures of SMBHBs across population parameter space. The grey dot-dashed line is the hard-binary limit (§2; Milosavljević & Merritt 2003) – below this line we consider SMBH pairs to be bound SMBHBs. Above this line the green x’s represent selected dual AGN candidates from Koss et al. (2023) and Goulding et al. (2019), as well as the most compact imaged AGN pair (7.3pc) from Rodriguez et al. (2006) (see §3.2.1 and Figure 2). The cyan region denotes where kinematically offset broad lines are detectable following Kelley (2021) and for binary mass ratio choices of $q = 0.05$ (larger triangle) and $q = 1$ (see §3.3.1). The blue-white shaded region is where periodic lightcurve candidates are detectable with present and upcoming optical time-domain surveys (see §3.4). The darker shading indicates where the binary residence time is longest (larger P) and the accreting binary would be the brightest (larger M). Magenta dots Graham et al. (2015b), orange x’s (Charisi et al. 2016), the black x (Liu et al. 2019), black +’s (Chen et al. 2020), and chartreuse stars (Chen et al. 2022b) denote photometric variability candidates from CRTS, PTF, Pan-Starrs, DES, and ZTF respectively (see §3.4.4 and §5.2). The thick yellow +’s indicate the first 13 helical jet candidates listed in §5.3, as identified by the methods described in §3.5. The red shaded triangle shows where direct orbital tracking techniques are effective (see §3.6). The purple shaded regions denotes where LISA (bottom left) and PTAs (middle right) are sensitive at the indicated redshifts. Unless otherwise specified, the binary mass ratio is assumed to be $q = 0.3$.

The angular separation of the binary on the sky, θ_{orb} , and the prospect of resolving it, depends on the distance to the binary, and its semi-major axis. The angular diameter distance at $z = 0.1$ is $D_A(z = 0.1) = 380 \text{ Mpc}$, while the majority of quasars will be at larger distances, with the quasar luminosity function peaking at $z = 2$, near distances of $D_A(z = 2) = 1.7 \text{ Gpc}$. Hence, in the best case scenario of a plausibly nearby, massive binary on a long period (but human-timescale) orbit, the angular scale of the orbit is,

$$\theta_{\text{orb}} = \frac{a}{D_A(z)} \approx 7.8 \mu\text{as} \left(\frac{P}{5.1 \text{ yr}} \right)^{2/3} \left(\frac{M}{10^9 M_\odot} \right)^{1/3} \left(\frac{D_A}{200 \text{ Mpc}} \right), \quad (9)$$

which is a factor of ~ 2.5 times smaller than the diffraction limited resolution of an Earth sized millimeter-wavelength very-long baseline interferometer (VLBI), *e.g.*, the Event Horizon Telescope. Hence, while directly resolving orbits is not impossible (§3.6), it is at the limit of present capabilities, and thus the vast majority of SMBHB search techniques rely on indirect detection methods.

What to look for? Viable observational signatures for identifying accreting SMBHBs must be clearly discernible from the signatures of their single SMBH counterparts. While the observational characteristics of accreting singles are often associated with normal quasar behavior, one cannot yet be certain if “normal quasar behavior” is the same as normal accreting-single-SMBH behavior. However, the above arguments, which suggest that sub-parsec SMBHBs are rare, also suggest that the quasar

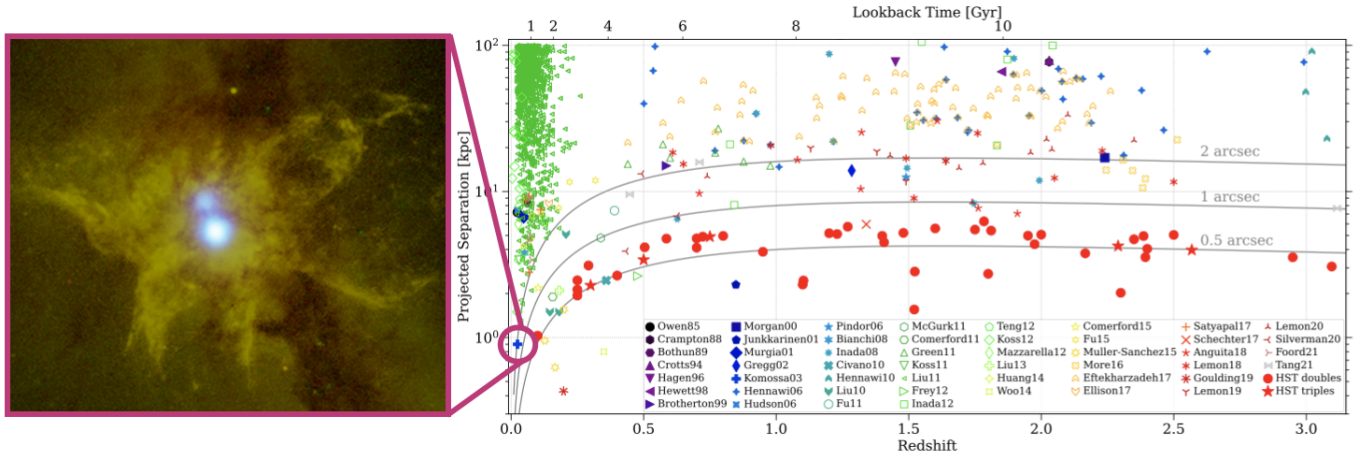


Figure 2. *Left:* One of the first dual AGN detected in the galaxy NGC 6240 with blue showing the X-ray emission from the SMBHs overlaid on optical image. *Right:* Dual AGN candidates plotted in separation and redshift space. Adapted from [Chen et al. \(2022a\)](#).

population on average has properties that represent the normal mode of single SMBH accretion, and that, if unique identifiable signatures of SMBHBs exist, they will be outliers among the quasars. The caveats here are that (1) our handle on the SMBHB population is orders of magnitude uncertain (although the recently discovered evidence for a nanohertz GW background by pulsar timing arrays (PTAs) already provides useful constraints, which will improve as PTAs better characterize the GW background spectrum—see §3.7), so in an extreme case, what we know about normal quasar activity could very much be tied to SMBHBs, and (2) most SMBHBs may simply not state their presence in the universe, or act observably very similarly to single SMBHs for most of their lives.

So how do we get beyond this? We must further develop (1) our understanding of the signal for which we are searching while (2) better characterizing the noise, in this case the behavior of “normal quasars” across temporal, wavelength, and spatial scales. For (2) we stress the importance of understanding the noise in order to measure a signal, but leave that for a different review. For (1), the topic of this chapter, we aim to identify signatures of SMBHBs that are (i) ubiquitous, *i.e.*, arising in a large fraction of SMBHB systems, and (ii) uniquely identifiable with SMBHBs. For the proposed signatures discussed below, the reader will see that it is difficult to fulfill both criteria, and when possible, it often requires observational techniques at the edge of our current abilities. We now review these approaches, paying attention to ubiquity and uniqueness, highlighting candidate systems when applicable, and compiling a candidate list organized by search method in §5.⁵

3.2. Macro-Scale Signatures and Evidence

At scales of kiloparsecs down to ~ 10 parsecs, we do have direct evidence for accreting SMBH pairs (dual AGN, §3.2.1). On these larger scales we also have circumstantial evidence that stellar interactions drive the two SMBHs together, potentially causing the brightness deficits observed in the cores of galaxies which are likely the products of major galaxy mergers (cored ellipticals, §3.2.2).

3.2.1. Dual AGN

The first stages of galaxy mergers and the pairing process of their SMBHs have been repeatedly observed as dual AGN. These are galaxies that have two active SMBHs, separated by kiloparsecs (and in a few cases by hundreds or tens of parsecs) and a few dozen of those have been resolved across the electromagnetic spectrum. Figure 2 provides a representation of known dual AGN (and dual AGN candidates) adapted from [Chen et al. \(2022a\)](#).

Despite the observational success of the last decade, dual AGN overall remain relatively rare and challenging to detect. Candidates are typically selected either serendipitously or through systematic searches and then verification methods are employed to confirm or exclude the presence of two SMBHs in the candidate galaxy. These typically involve observationally demanding multi-wavelength follow-ups. One of the main challenges in the quest for dual AGN is the inherent observational trade-off between large field of view (required to build large samples of AGN) and high resolution (crucial for confirming the dual AGN).

⁵ We do not attempt a complete list of present-day candidates, but note that the existence of a living database of candidates as they gain more evidence for or against their candidacy would be useful to the field (*e.g.*, [Sydnor et al, in prep](#)).

For instance, mid-infrared (IR) surveys, like WISE, have covered the entire sky detecting millions of AGN but their resolution is extremely limited, while at the other end, VLBI has exceptional resolution but cannot survey the sky and is only suitable for detailed follow-ups. Similarly high-resolution telescopes like Chandra and HST have only covered a small fraction of the sky. Another major challenge is the high degree of bias in the detected samples, which is hard to account for. Since systematic searches typically pre-select candidates by compiling a large sample of AGN, and then identifying a promising dual signature, they can be significantly biased (*e.g.*, mid-IR methods preferentially select star-forming, dusty AGN, whereas X-ray methods prefer AGN with lower gas content, [Azadi et al. 2017](#); [Stemo et al. 2020](#)). Hence, the observed sources are not necessarily representative of the underlying population, which complicates the connection with the galaxy mergers and the occurrence of binaries at smaller separations.

We emphasize, however, that the detection of dual AGN has significantly advanced our understanding of galaxy formation and evolution and can offer insights into observational strategies to detect sub-parsec binaries. For this reason, here we briefly summarize some of the observational highlights, but we refer the reader to [De Rosa et al. \(2019\)](#) for a detailed review.

In one method, candidates are selected in the vast spectroscopic database of SDSS by searching for double-peaked emission lines (*e.g.*, primarily [OIII], but also [NeV] and [NIII]), which reflect the motion of the AGN in the common gravitational potential, assuming that each AGN carries its own narrow emission line region ([Wang et al. 2009](#); [Liu et al. 2010](#); [Comerford et al. 2013](#)). However, because this signature is not unique and other kinematic effects, such as outflows or rotating gas disks, can result in similar profiles ([King & Pounds 2015](#); [Nevin et al. 2016](#)), additional data are required to confirm the existence of two SMBHs in the host galaxy. Detailed optical imaging with the Hubble Space Telescope and Keck, along with integral-field unit (IFU) spectroscopy, have confirmed that $\sim 2\%$ of the candidates are indeed dual AGN ([Fu et al. 2011](#); [McGurk et al. 2015](#); [Liu et al. 2018b](#)). We note that IFU spectroscopy can also provide a good alternative for candidate identification, but it is typically demanding and is only accessible from a limited set of telescopes. JWST is extremely promising in this regard (since MIRI and NIRCAM are equipped with IFU) and is expected to rapidly increase the number of known dual AGN.

Beyond the optical band, X-ray imaging and spectroscopy have also uncovered several dual AGN systems, especially in obscured galaxies. X-ray observations have either targeted candidate systems described above or have focused on fields with extensive coverage (*e.g.*, COSMOS, Chandra Deep Fields) leveraging multi-wavelength data to uncover dual AGN candidates. Additionally, a number of dual AGN have been discovered serendipitously ([Komossa et al. 2003](#); [Koss et al. 2011](#); [Foord et al. 2019](#)). Currently, Chandra has the best spatial resolution of one arcsecond in X-rays and can resolve dual AGN systems with separations down to ~ 8 kpc at $z = 1$ (or ~ 1.8 kpc at $z = 0.1$). Note that Chandra’s resolution decreases off axis but can be improved with advanced statistical methods like BAYMAX ([Foord et al. 2019](#)).

The highest overall spatial resolution of order milli-arcseconds can be achieved in radio bands with VLBI, allowing the detection of dual AGN down to 10 parsecs and even smaller in the local universe (see also §3.6). One limitation to this is that both AGN should be bright in radio wavelengths, which may be rare; in general radio-loud AGN are $<10\%$ of the population (*e.g.*, see [Müller-Sánchez et al. 2015](#) on dual AGN verification with radio follow-ups). In addition, because VLBI has a narrow field of view, it is most suitable to study pre-selected promising individual objects or small samples of candidates. This method has returned the record-holding binary at a projected separation of 7.3pc ([Rodríguez et al. 2006](#)), in which the relative motion of the two SMBHs has also been observed ([Bansal et al. 2017](#)).

Detection of sub-kiloparsec dual AGN (10pc-1kpc) can also be achieved through precision astrometry paired with variability (*e.g.*, [Popović et al. 2012](#)). This method, recently referred to as varstrometry, tracks the photocenter of light coming from both AGN and host-galaxy light. As one or both AGN vary in brightness due to intrinsic (or possible binary induced) variability, the photocenter changes, allowing one to probe photocenter offsets between components ([Shen et al. 2019](#); [Hwang et al. 2020](#); [Chen et al. 2022a](#)).

3.2.2. Cored Ellipticals

As discussed in §2, an important mechanism for hardening SMBHBs is stellar interactions, whereby SMBHB angular momentum and energy is traded to stars on initially centrophilic orbits, kicking them out of the central region of the stellar core which surrounds the SMBHB. For this reason, [Begelman et al. \(1980\)](#) first pointed out that the stellar core of a galaxy that recently harboured an SMBHB merger should have a deficit of stars within the hardening radius of the binary (grey-dot-dashed line in Figure 1 where the binary orbital velocity matches the stellar velocity dispersion, see also, [Milosavljević et al. 2002](#); [Ebisuzaki et al. 1991](#)). Such stellar cores are indeed found in the brightness profiles of some elliptical galaxies ([Lauer 1985](#); [Kormendy & Ho 2013](#)), though it is difficult to provide direct proof that cored ellipticals are created by SMBHB scouring. For example, AGN feedback from single-SMBH accretion has been proposed (*e.g.*, [Martizzi et al. 2013](#)) as an alternative culprit. However, convincing evidence for the binary picture has been mounted. Namely: (1) Mass deficits predicted by binary+stellar hardening

theory match the measured central SMBH mass in cored ellipticals (Merritt 2006; Kormendy & Bender 2009). (2) The core size matches the SMBH sphere of influence, derived from measured SMBH and stellar properties (Thomas et al. 2016). (3) Anisotropic velocity dispersions observed in cored ellipticals could be caused by preferential removal of stars on highly radial orbits during the scouring process (Rantala et al. 2018).

Pros and Cons: Macro-Scale Signatures

Pros:

- We have successfully observed dozens of double AGN sources, and cored ellipticals.
- Prospects with the James Webb Space Telescope or future high energy telescopes with high resolution like LynX are promising.

Cons:

- Multi-wavelength follow-ups for dual AGN are observationally demanding.
- Dual AGN samples are not complete and selection effects hinder the extraction of physical quantities like the rate of dual AGN in galaxies or relevant timescales.
- Due to uniqueness problems, it is not clear if one can tie the rate of stellar hardened SMBHB pairings to the cored ellipticals.

3.3. Spectral Signatures

The idea for using spectral features to detect SMBHBs was prompted first by observations of broadened emission lines offset in redshift from narrow emission lines in the then newly discovered quasars (Kormberg 1968; Gaskell 1983, very likely inspired by a history of using spectra to identify binary stars in astronomy). This has led to a long tradition of searching for offset, variable, and double peaked broad emission lines as evidence for SMBHB orbital motion, which we discuss in §3.3.1. In addition to broad line signatures, advances in modeling accretion onto binaries has led to other proposed spectral signatures arising from more indirect outcomes of a binary orbital motion, such as clearing of gaps and cavities in circumbinary accretion disks. We discuss signatures of these processes occurring much closer to the SMBHBs in subsection §3.3.2.

3.3.1. Broad Line Features and Variability

Gas ionized by the central power source of AGN, i.e. the accreting SMBH(s), emits a multitude of emission lines at different atomic transitions. The width of the so-called broad emission lines is due to Doppler broadening caused by orbital motion of gas around the central mass, while emission from much more slowly orbiting gas farther from the central source is not greatly broadened, resulting in reference narrow lines (see, e.g., Osterbrock & Mathews 1986, for a classic review of emission lines in AGN). Offsets of $\sim 10^3$ km/s (up to 5,000 km/s) in redshift between broad and narrow line centers could suggest that the broad line region is coherently moving, because it is bound to a component of a binary and so red- or blue-shifted by the SMBHB orbital velocity (see Figure 3).

Early studies (before 2010) focused on interesting individual sources with peculiar spectral features (Kormberg 1968; Gaskell 1983; Stockton & Farnham 1991; Gaskell 1996; Bogdanović et al. 2009; Dotti et al. 2009; Boroson & Lauer 2009; Decarli et al. 2010; Barrows et al. 2011; Bon et al. 2012). Subsequently, the vast spectroscopic dataset of SDSS enabled many systematic searches for binary broad line signatures (Tsalmantza et al. 2011; Eracleous et al. 2012; Shen et al. 2013; Ju et al. 2013; Liu et al. 2014b), see also §5.1. These signatures can be roughly sorted into three categories:

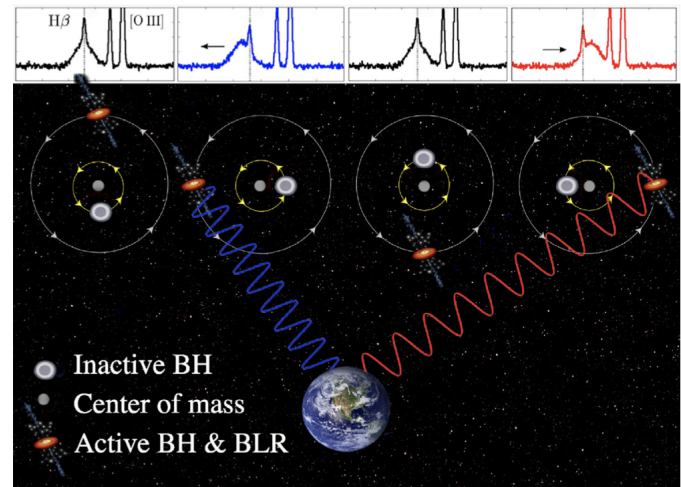


Figure 3. Cartoon showing the expected Doppler shift in broad emission lines, induced by the motion of the binary, assuming that only one SMBH is active and carries its own broad line region. The expected coherent modulation in radial velocity provides a required test for binarity but the timescales for this are long. From Guo et al. (2019).

- *Broad lines kinematically offset with respect to the narrow lines identified through single-epoch spectroscopy.* The narrow emission lines are produced at large distances from the galactic nucleus and are not affected by the presence of a binary, thus tracing the rest-frame of the galaxy. If one of the binary components accretes at a higher rate than the other and carries with it the only broad line region of the system, the broad emission lines will be displaced compared to the narrow lines, due to the orbital velocity of the SMBH (Dotti et al. 2009; Tsalmantza et al. 2011; Eracleous et al. 2012; Liu et al. 2014b).
- *Broad lines varying in offset (or shape) over time identified through multi-epoch spectroscopy.* The broad line variability may arise in a binary system if each SMBH has its own broad line region or if only one of the SMBHs is accreting (Shen et al. 2013; Ju et al. 2013; Wang et al. 2017). This method has the advantage of detecting candidates at a variety of orbital phases, even when the line-of-sight radial velocity is zero (which would have been missed in single-epoch searches) since at that phase the line-of-sight acceleration is maximum. These searches attempted to provide the first constraints on the fraction of quasars hosting binaries, but the range is wide (from 1% to almost all quasars being associated with binaries) and dependent on assumptions about the unknown physics of broad line regions. Additionally, most of the candidates identified from single-epoch spectroscopy were subsequently monitored to search for coherent changes in the radial velocities, as expected in the binary scenario (Eracleous et al. 2012; Decarli et al. 2013; Liu et al. 2014b; Runnoe et al. 2015, 2017). Some of the candidates have evolving radial velocities consistent with the orbital motion of a binary or have led to constraints on the binary parameters (Runnoe et al. 2017; Guo et al. 2019), while others have already been ruled out due to lack of variability or due to radial velocity curves inconsistent with the orbital motion of a binary (Wang et al. 2017; Guo et al. 2019).
- *Double-peaked broad lines* may be caused by two broad line regions, each bound to one of the black holes in the binary. Multiple candidates have been considered over the years, especially in the earlier days of the field, (Stockton & Farnham 1991; Eracleous & Halpern 1994; Boroson & Lauer 2009; Tsai et al. 2013), but follow-up studies disfavored the binary interpretation of these systems, (*e.g.*, see Eracleous et al. 2009; De Rosa et al. 2019, for reviews), and they may be more simply generated by single AGN disks (*e.g.*, Eracleous et al. 1997; Eracleous & Halpern 2003; Liu et al. 2016; Doan et al. 2020). This signature is also challenging from a theoretical perspective; the proper balance of line width and offset required for such a splitting to be observable places strict requirements on the allowed orbital parameters (Shen & Loeb 2010; Kelley 2021).

Kinematically offset broad lines are detectable for binary separations ranging from ~ 0.1 pc to ~ 10 pc (see cyan region in Figure 1), while systems for which time changing offsets are detectable make up a smaller portion of parameter space. The binary separation must be small enough (and the orbital velocity large enough) to detect offsets due to orbital motion (Eracleous et al. 2012; Ju et al. 2013; Pffueger et al. 2018; Kelley 2021), and the binary must also be close enough to be gravitationally bound if Keplerian evolution of the line offsets is to be expected. The above signatures also require that the binary is wide enough that at least one of its components can hold onto a bound, luminous broad line region (Runnoe et al. 2015; Kelley 2021). From these considerations, Kelley (2021) estimates that for contemporary observational capabilities, kinematic offsets are detectable for $\sim 0.5\%$ of a mock SMBHB population, for those with total masses $\gtrsim 10^7 M_\odot$ and separations between 0.1 and 10 pc. The cyan region in Figure 1 depicts the portion of parameter space where these criteria are met (Eqs. (6) and (10) of Kelley 2021 with $f_{\text{Edd}} = 0.1$), assuming 10^3 km/s broad line offsets due to orbital motion of the secondary SMBH, and assuming mass ratios of $q = 0.05$ and $q = 1.0$ (large and small cyan triangles, respectively, in Figure 1) to bracket the range of binary masses and periods that allow such offsets. Changes in the kinematic offsets will only be detectable for the shorter orbital period systems in the cyan region of Figure 1, estimated to constitute 0.03% of the mock SMBHB population in Kelley (2021).

Recent modeling has considered circumbinary broad-line regions which could exhibit time-dependent line profiles and centroids due to the changing illumination pattern of the central binary (Bogdanović et al. 2008; Shen & Loeb 2010; D’Orazio et al. 2015a; Nguyen & Bogdanović 2016; Nguyen et al. 2019, 2020; Ji et al. 2021a). Such signatures would exist in a extended part of parameter space, at smaller binary separations, where an intact broad-line region need not be bound to either binary component. However, comparison of recent model line profiles by Nguyen et al. (2019) and Nguyen et al. (2020) between a sample of SMBHB candidates and a control sample shows that the inferred putative binary parameters between the two sets are indistinguishable. Hence, such a diagnostic may be useful for inferring parameters of known SMBHBs, but not for identifying them. While predictions for the circumbinary-broad-line response are less certain and possibly not unique to an SMBHB, correlation with photometric variability could help with uniqueness arguments. Correlation of the changing circumbinary-broad-line shapes and magnitudes with the photometric variability of continuum emission (*e.g.*, §3.4) could offer a promising handle for testing the binary hypothesis and mapping broad-line regions (Ji et al. 2021b).

3.3.2. Circumbinary Disk Spectral Features

Another class of possible spectral signatures from accreting SMBHBs arises from the inner binary accretion flow itself. The idea is as follows: the spectrum of a standard steady-state accretion disk around a single black hole is found from solving for the disk radial temperature profile and summing the multi-component black-body emission from each radial ring (Shakura & Sunyaev 1973). In the case of circumbinary accretion, however, the temperature profile (and even the optically thick, blackbody assumption) can be modified. For example, the disk surface density snapshots in Figure 5, for binaries of different mass ratios, show that the binary can clear a low density ring or cavity in the disk. At first approximation, this could result in lack of emission at these radii, and possibly a deficit (or ‘notch’) in the equivalent single-SMBH-disk spectrum (Gültekin & Miller 2012; Roedig et al. 2014). Other consequences of the cavity include softer than expected spectral energy distributions, weaker broad lines (Tanaka et al. 2012), or spectral edges caused by Lyman- α absorption at the inner edge of the cavity (Generozov & Haiman 2014).

Following the above predictions, Yan et al. (2015) proposed an SMBHB candidate with separation of ~ 3 milli-parsec based on an observed optical-UV deficit in the spectrum of the nearby quasar Mrk 231 (but see Leighly et al. 2016, who suggested that the observed spectral features are due to dust-reddening). Guo et al. (2020) searched for predicted spectral energy distribution truncations or peculiarities in a set of 138 candidate SMBHBs identified by periodic brightness variations (see §3.4). Six systems showed abnormally red, blue-truncated spectra that are consistent with empty-cavity circumbinary disk spectral energy distribution models. However, this fraction is consistent with the fraction of similar outliers in a control sample, and could also be explained via dust-reddening. Foord et al. (2022) examined spectra for the SMBHB candidate SDSS J025214.67-002813.7, identified by periodic brightness variations (Liao et al. 2021). Compared to standard AGN SEDs, this system exhibits excess soft X-ray emission in the 0.5 – 10 Kev range and a blue deficit above 1400 Å. However, to explain the latter, a dust reddening model is preferred over a binary hypothesis.

In addition to reprocessing or adjusting single-disk emission, a more sophisticated treatment of the binary accretion problem will also result in an underlying spectrum that deviates from the single SMBH case. For example, binary torques will contribute a heating term to the energy balance that can change the disk temperature profile. Manifestations of this are evident in, e.g., Roedig et al. (2014), which predicted an X-ray excess due to Compton cooling in shocks generated as streams from the circumbinary disk hit the disks around each SMBH (often referred to as circumsingle or mini-disks; see Figure 5). The numerical calculations of Farris et al. (2015b); Tang et al. (2018); Westernacher-Schneider et al. (2022); Ryan & MacFadyen (2017) lend further support for high-energy excesses due to gas dynamics and shocks in the inner region of the circumbinary disk and mini-disks, albeit due to different physical reasoning.

The latter works carried out viscous hydrodynamical simulations with simple optically thick radiative cooling. In reality, the optically thick assumption (and hence radiatively efficient blackbody cooling assumption) may break down in the cavity, and result in different cooling mechanisms and different spectra. For example, D’Orazio et al. (2015b) argue that for the SMBHB candidate PG 1302-102 (see §3.4.2), the accretion flow onto the putative binary should be a combination of radiatively efficient (optically thick black body, e.g., Shakura & Sunyaev 1973) and advection dominated accretion flows (e.g., Narayan & Yi 1995), allowing the possibility for more complex spectral signatures. While such composite binary accretion flows have not yet been simulated, d’Ascoli et al. (2018); Gutiérrez et al. (2022) carry out general relativistic magneto-hydrodynamical (GRMHD) simulations near merger that implement an ad-hoc cooling mechanism which cools towards a target entropy and reconstructs spectral energy distributions assuming black-body emission in the bulk, optically thick regions of the disk and an inverse Compton scattering emissivity in the optically thin cavity. In these simulations the inverse Compton emission from the cavity and SMBH mini-disks results in a high-energy coronal type component of the SMBHB spectrum. Saade et al. (2020) provide a more detailed overview of predicted high-energy (X-ray) features of accreting SMBHBs, motivating searches for peculiar X-ray spectral indices or abnormal X-ray-to-optical flux ratios (compared to the known AGN population) as indicators of SMBHB accretion. To date, a handful of SMBHB candidates with X-ray and optical observations have been examined under this light, but no significant abnormalities have been found (Saade et al. 2020; Hu et al. 2020; Saade et al. 2023).

Finally, McKernan et al. (2013) show that it is not only the spectral energy distribution that can be affected by gaps and cavities in circumbinary accretion disks, but also the shape of the Fe K- α spectral line, which appears in X-rays (at 6.4-7keV, rest frame) and probes the inner regions of SMBH(B) accretion disks (Fabian et al. 2000). McKernan et al. (2013) predict oscillations in the line shape due to Doppler boosting as well as missing wings (red and blue extremes) of the line due to cavity or gap formation. Such features may be observable with next-generation X-ray observatories such as Athena (Nandra et al. 2013). No Fe K- α lines were detected in the Chandra follow-up observations reported in Saade et al. (2020), which is typical for such AGN at the reported count rates.

Pros and Cons: Spectral Signatures

Pros:

- Spectroscopic databases like SDSS have provided large samples of quasars allowing for systematic searches, which have revealed many promising candidates.
- The time-domain component of SDSS-V, Black Hole Mapper, is well suited to uncover more candidates.
- The most widely separated binaries detected with this method can be resolved with VLBI if both components are radio loud (See §'s 3.2.1 and §3.6).
- Long term monitoring can provide stringent constraints on the binary parameters and potentially exclude the binary hypothesis.

Cons:

- The signatures are not unique to SMBHBs.
- The more unique, Fe K- α signatures are much harder to observe for any but the brightest AGN.
- For the traditional (optical) broad line signatures in the beginning of §3.3.1, binary periods are long (decades to centuries) and thus observing a full orbit is hard and confirmation of binarity challenging.
- This signature likely probes a small part of SMBHB orbital parameter space (Figure 1).

3.4. Photometric Signatures (Periodic Variability)

The primary idea behind the periodic variability method is that the difference between accreting single SMBHBs and binaries can be borne out from periodic brightness variations in the lightcurves of quasars powered by binary accretion (Haiman et al. 2009). This periodicity is imprinted, in some way or another, by the periodic orbital motion of the gravitational two-body problem.

Regardless of the process which imprints periodicity, the timescale is set by the binary orbital period and its multiples. SMBHBs with masses between $10^7 - 10^{10} M_{\odot}$, with 0.01 pc separations, at redshift z , have observer-frame orbital periods ranging from $\sim 30(1+z)$ to $\sim 1(1+z)$ yr, and can be observed out to high redshifts when accreting near the Eddington rate.⁶ In this Section we review how periodic orbital motion can be imprinted on observed emission from binary accretion, the status of observational searches, and challenges in detecting such signals.

3.4.1. Hydrodynamical Variability

Theoretical and numerical models of circumbinary accretion have shown that the time-averaged accretion rate onto the components of a binary matches that expected onto a single point mass of equivalent mass (e.g., D’Orazio et al. 2013; Farris et al. 2014). In cases studied so far, torques from the binary on the inflowing circumbinary gas do not inhibit accretion onto the individual components (see, however, Ragusa et al. 2016, but also Dittmann & Ryan 2022). Therefore, binary-powered accretion can be as bright as accretion powered by a single SMBHB.

Moreover, numerical studies show that the accretion rate onto the binary can be strongly modulated at the binary orbital period and multiples thereof. A landscape of accretion-rate variability arises with strong dependence on binary parameters. The left panel of Figure 4 shows an accretion-rate time series for an equal-mass binary in a circular orbit, while the right panel shows a periodogram of accretion rate variability for a range of circular orbit mass ratios (Duffell et al. 2020). For binaries on circular orbits, a trend with binary mass ratio q arises (D’Orazio et al. 2013; D’Orazio et al. 2016), and can be split into three regimes:

- **Three-timescale regime ($q \gtrsim 0.2$):** The binary modulates the accretion flow at the orbital period and twice the orbital period by periodically pulling in streams from the circumbinary disk. For exactly equal mass binaries periodicity at the orbital period disappears due to symmetry. The majority of material from these streams is flung back out into the circumbinary disk maintaining a low-density central cavity (e.g., Tiede et al. 2022). This cavity becomes eccentric with a side near the binary, from which it pulls streams and accretes most strongly, and a side far from the binary into which the majority of stream material is ejected by the rapidly rotating binary potential. An overdensity (often referred to as the “lump”) develops due to coherent impacts from streams that enter the cavity and are subsequently expelled back out hitting the far side of the cavity wall ($(2 - 4a)$, see description in D’Orazio et al. 2013). This overdensity, labeled in Figure 5, builds up and then orbits at the local Keplerian frequency. Streams heading toward collision with the cavity wall, which re-enforce the overdensity, are also visible in the right panel snapshot in Figure 5. Once every ≈ 5 binary orbits, the

⁶ LSST of the Rubin Observatory should detect SMBHBs with masses $> 10^6 M_{\odot}$ accreting at 0.1 Eddington for $z \leq 1$.

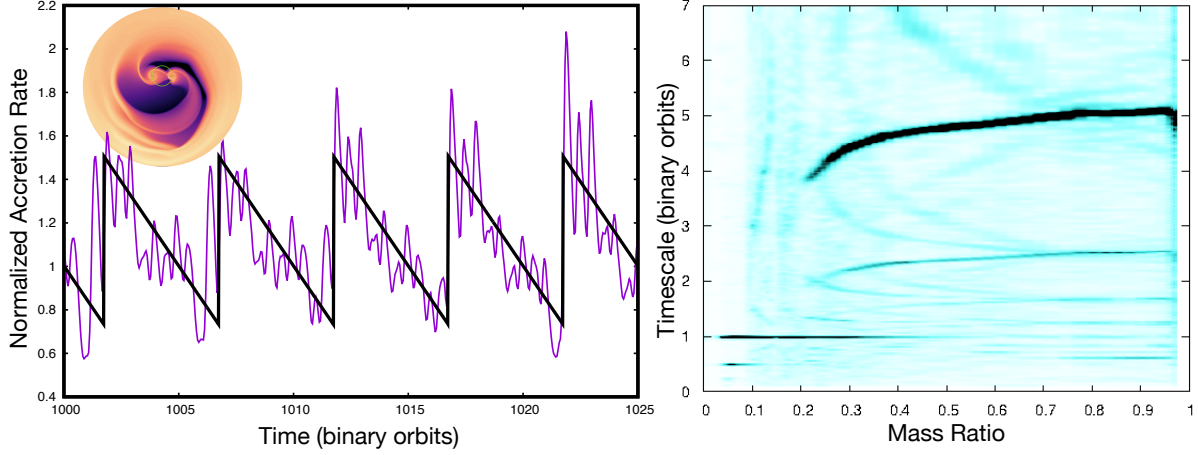


Figure 4. *Left:* Simulation measured accretion rate (purple) over 25 orbits for an equal mass binary on a circular orbit (adapted from Duffell et al. 2020). The inset is a snapshot of log surface density in a disk simulation from which the accretion rate is measured. *Right:* A 2D periodogram of the accretion rate time-series for binary mass ratios spanning 0.01 to 1.0 (adapted from Duffell et al. 2020). For low mass ratios, periodic variability at the binary orbital period is dominant. For near-equal mass ratios, periodicity at a combination of the binary orbital timescale, a five times longer periodicity, and harmonics all are present.

orbiting overdensity reaches the side of the cavity that comes nearest to the binary and causes an overfeeding, temporarily increasing the accretion rate onto the binary. As can be seen in the periodogram of Figure 4, this super-orbital periodicity dominates for near-unity mass ratios. This feature does not always arise (see below), but is seen in numerical calculations that use a range of techniques and include a range of physics, *e.g.*, non-trivial thermodynamics, magneto-hydrodynamics (MHD), self-gravity, 2D and 3D (MacFadyen & Milosavljević 2008; D’Orazio et al. 2013; Noble et al. 2012; Shi et al. 2012; Shi & Krolik 2015; D’Orazio et al. 2016; Muñoz et al. 2019; Moody et al. 2019; Ragusa et al. 2020; Noble et al. 2021).

- **Orbital-timescale regime ($0.05 \lesssim q \lesssim 0.2$):** Below approximately $q = 0.2$, the orbiting overdensity cannot be maintained and the super-orbital $\sim 5P$ periodicity vanishes leaving only power at the orbital period and twice the orbital period (middle panel of Figure 5 and right panel of Figure 4). Even though the lump formation seems to be robust across many different calculations, the criteria for its formation/destruction is an active area of research (*e.g.*, Noble et al. 2021; Mignon-Risse et al. 2023) and is likely dependent not only on the mass ratio, but on disk properties and thermodynamics (Sudarshan et al. 2022; Wang et al. 2023a,b).
- **Steady regime ($q \lesssim 0.05$):** For small mass ratios, the accretion-rate variability becomes low-amplitude and stochastic (left panel of Figure 5). This transition is coincident with a range of mass ratios near where the loss of stable co-orbital orbits occurs in the restricted three body problem ($q \geq 0.04$), but also has dependence on disk properties (D’Orazio et al. 2016; Dittmann & Ryan 2023).

Accretion variability for eccentric, near equal mass ratio binaries is qualitatively similar to the circular orbit case for $e \lesssim 0.1$. For more eccentric binaries, however, the orbiting overdensity that generates the dominant super-orbital periodicity disappears, leaving an accretion rate dominated solely by the orbital timescale and its harmonics. The shape of the accretion rate modulation also changes with higher eccentricity, becoming more bursty, with a peak just preceding the time of binary pericenter (Zrake et al. 2021; Muñoz & Lai 2016; Dunhill et al. 2015, D’Orazio & Duffell, In prep.). A systematic exploration of accretion rates for eccentric binaries with disparate mass ratios has been recently carried out by Siwek et al. (2023).

Much of the above picture has been realized using numerical viscous-hydrodynamical and MHD calculations with relatively simple or isothermal gas-cooling prescriptions and for a relatively narrow range of disk parameters. For example, the equilibrium disk aspect ratio which controls pressure forces, rarely deviates from the range 0.1 – 0.03 in these calculations (Tiede et al. 2020), despite expectations from radiatively efficient, steady-state disk theory that this value should fall below 0.01 for accretion onto SMBHs (Shakura & Sunyaev 1973; Sirko & Goodman 2003; Thompson et al. 2005). However, recent parameter studies have found that the three-timescale regime above is relatively robust over a range of disk aspect ratios and viscous magnitudes (Dittmann & Ryan 2022), with Dittmann & Ryan (2023) finding accretion rate variability down to $q = 10^{-2}$ for thinner disks.

These choices for disk properties control when, for example, the orbiting overdensity can be sustained and so control the boundaries between the above regimes. Even so, comparison with observed accretion rates onto stellar binaries has been carried out with reasonable success (Tofflemire et al. 2017). Though extrapolation to the SMBH case may not be straightforward because in the stellar case the disk aspect ratio is expected to be closer to the widely simulated values of ~ 0.1 , and buffering of accretion rate variations by the mini-disks may be less important due to the larger physical extent of the stars or their magnetospheres. Finally, note that misalignment of the circumbinary disk with the binary will likely also alter this landscape of accretion variability (Moody et al. 2019; Doğan et al. 2015; Smallwood et al. 2022).

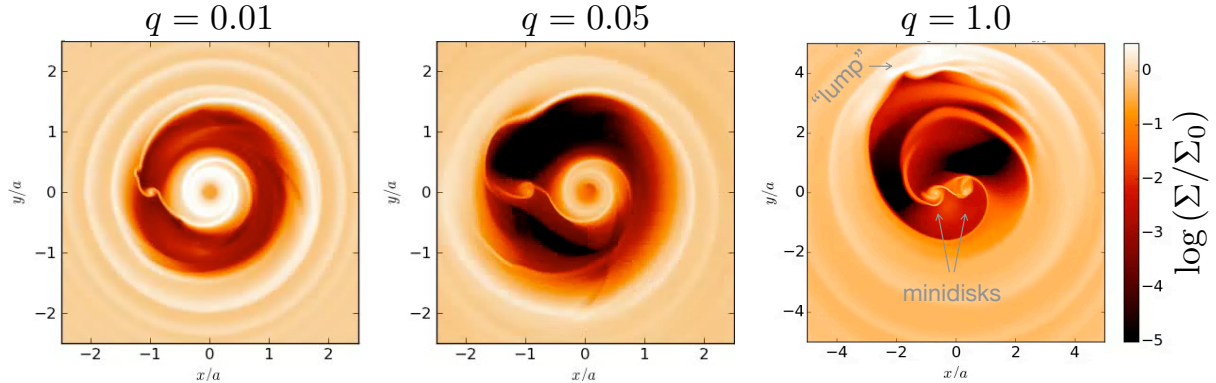


Figure 5. Log surface density snapshots of numerical calculations described in D’Orazio et al. (2016), for different binary mass ratios $q = M_2/M_1 \leq 1$. These snapshots correspond to the three accretion-rate variability regimes for circular orbit binaries. The binaries are orbiting counter-clockwise.

While the accretion rate sets the spectrum and luminosity of a steady-state disk, it is not clear that the observed luminosity will exactly track variations in simulation-measured accretion rates. The accretion rate varies on the orbital timescale while a separate timescale controls how quickly this translates into a change in observed emission. This latter timescale may be set by the viscous time in the mini-disks surrounding each SMBH, the photon diffusion time required for a changing disk temperature to propagate to the disk photosphere, or other timescales relevant to the dominant form of radiative cooling. If these timescales are longer than the orbital period, then a resulting buffering of the accretion rate variability could result in diminished or no variability in the observed flux (e.g., Bright & Paschalidis 2023).

A few studies have solved the energy equation with a cooling prescription in order to track not just the accretion rate, but a (sometimes) frequency dependent luminosity. 3D GRMHD simulations of $\mathcal{O}(10)$ binary orbits near merger (d’Ascoli et al. 2018; Gutiérrez et al. 2022), with the HARM3d code (Noble et al. 2009) include an ad-hoc cooling function and post-process the resulting disk radiation in the binary black hole spacetime, finding variability signatures in the disk emission. Other studies implement a simple optically thick black-body cooling function and find that the luminosity generally tracks the accretion rate (Farris et al. 2015b; Tang et al. 2018; Westernacher-Schneider et al. 2022). Using tuneable β -cooling prescriptions, Sudarshan et al. (2022); Wang et al. (2023a,b) find that slower cooling rates can result in drastic changes in disk response, which can result in the loss of accretion variability, depending on the adopted viscosity prescription.

Overall, numerical simulations have shown that binaries can accrete at a high rate and can generate time variable, quasi-periodic accretion rate modulations, which can be translated into observed luminosity modulations. The shape of these time-series modulations and the dominant variability timescales depend on binary and disk properties. In some cases, periodic variability may be lost altogether. To prepare to interface with observations of accreting binaries, we require a more complete study of binary accretion. Specifically, numerical studies need to provide output appropriate for generating synthetic observations. At minimum, this should include 3D and more sophisticated treatment of the energy equation to allow for accurate inclusion of the evolution of and emission from optically thin regions such as may be found in the circumbinary disk cavity (see Figure 5). This must also be carried out for a range of binary and disk parameters.

Binary Tidal Disruption

A subset of hydrodynamical variability signatures caused by binary accretion could come from the tidal disruption of a star by one of the SMBHs in a compact, sub-parsec separation binary. Such tidal disruption events (TDEs) might be expected if stellar

hardening is responsible for SMBHB orbital evolution. The stellar disruption could serve as a fuel source for a circumbinary disk (Coughlin & Armitage 2017), or fall directly onto one of the black holes resulting in a TDE lightcurve that can be dramatically altered by the second black hole, for short orbital period SMBHBs. Large dips and excesses, or possibly periodic Doppler boosting (discussed below), on top of a decaying TDE lightcurve could help to identify the SMBHB (Liu et al. 2009; Ricarte et al. 2016; Hayasaki & Loeb 2016; Coughlin et al. 2017).

The probability of detecting such an event and the effect of the SMBHB on the TDE lightcurve is dependent on the binary separation (Coughlin et al. 2019). At large separations, when one SMBH first strongly perturbs the stellar distribution bound to the other SMBH, the rate of TDEs can grow by 2-3 orders of magnitude over the single SMBH rate (see Chen et al. 2011; Lezhnii & Vasiliev 2019, and reference therein). Apart from indirectly inferring a high TDE rate in a single galaxy type (e.g., E+A galaxies Arcavi et al. 2014; French et al. 2016), these disruptions by widely separated SMBHBs likely look no different than a TDE onto a single SMBH. Anyway, after $\mathcal{O}(\text{Myr})$ the reservoir of available stars is quickly depleted and the TDE rate drops below the equivalent single SMBH rate (Coughlin et al. 2019). The rate can again increase by a factor of few to ten if the binary reaches \lesssim milli-parsec separations (Coughlin et al. 2017; Darbha et al. 2018). At this stage, the binary orbital period becomes of order the stellar debris fallback time, allowing manifestation of the possibly identifiable binary signatures listed above. However, the enhanced TDE rate here may be mitigated by a shorter window of detectability set by the $\mathcal{O}(10^3 - 10^9)\text{yr}$ lifetimes for SMBHBs with $M = 10^8 - 10^6 M_\odot$, respectively. Candidate TDEs in binary systems have been proposed in the literature (Liu et al. 2014a; Coughlin & Armitage 2018; Shu et al. 2020), each, however, with competing explanations (e.g., Grupe et al. 2015; Leloudas et al. 2016; Margalit et al. 2018; Coughlin et al. 2018).

3.4.2. Orbital Doppler Boost and Binary Self-Lensing

Even in the case that accretion rate variations are not excited by the binary (e.g., $q \lesssim 0.05$) or are not translated into luminosity variations, periodic variability is expected to occur due to relativistic, observer-dependent effects when emitting gas is bound to one or both SMBHs in the binary. These include the relativistic Doppler boost caused by line-of-sight components of the orbital velocity, and binary-self-lensing, i.e., the periodic gravitational lensing of light from one SMBH's accretion disk by the other SMBH.

Orbital Doppler Boost

The Doppler boost results in the luminosity of a source appearing brighter and bluer (or dimmer and redder), when the line-of-sight velocity is pointed towards (or away) from an observer. We briefly derive the expected Doppler boost variability (see also Charisi et al. 2022, for a similar derivation). For a single, isotropically emitting source, the observed and emitted (primed frame) specific fluxes are related by

$$F_\nu = D^{3-\alpha_\nu} F'_\nu, \quad (10)$$

where we have assumed additionally that the emitted spectrum of the source is a power law, $F'_\nu \propto \nu^{\alpha_\nu}$, over the observing band with log slope $\alpha_\nu = \ln F'_\nu / \ln \nu$.

The Doppler factor D is the ratio of observed and emitted frequencies,

$$D \equiv \frac{\nu}{\nu'} = \frac{1}{\gamma(1 - \beta \cdot \hat{\mathbf{n}})}, \quad (11)$$

and depends on the Lorentz factor γ and the line-of-sight velocity of the source $\beta \cdot \hat{\mathbf{n}}$ in units of the speed of light.

Assuming a circular binary orbit with inclination I measured from face-on, and expanding to first order in the orbital velocity β_{orb} , the observed flux is,

$$F_\nu = (3 - \alpha_\nu) \left[1 + \beta_{\text{orb}} \cos \left(\frac{2\pi t}{P} \right) \sin I \right] F'_\nu, \quad (12)$$

which is a sinusoid with the same period as the orbit, P , and amplitude,

$$A_\nu = (3 - \alpha_\nu) \beta_{\text{orb}} \sin I. \quad (13)$$

Writing β_{orb} for the secondary SMBH in the binary and in terms of number of Schwarzschild radii $N_a \equiv a/(2GM/c^2)$, $\beta_{\text{orb}} = [(1+q)^2 2N_a]^{-1/2}$, which for SMBHBs at sub-parsec separations, corresponds to a few % to a $\sim 10\%$ amplitude modulation in the lightcurve (see left panel of Figure 6), which is easily observable with ground-based photometry, given that other sources of variability do not swamp the signal (see §3.4.4). In the above, we assume one emitting source e.g., one of the

mini-disks dominates the variability, typically the mini-disk of the secondary which also moves at higher velocities. If both mini-disks are Doppler boosted, since the two SMBHs are moving in opposite directions, the motion of one will lead to an increase in luminosity, while, at the same time, the motion of the other will have a dimming effect, diminishing the overall amplitude of variability.

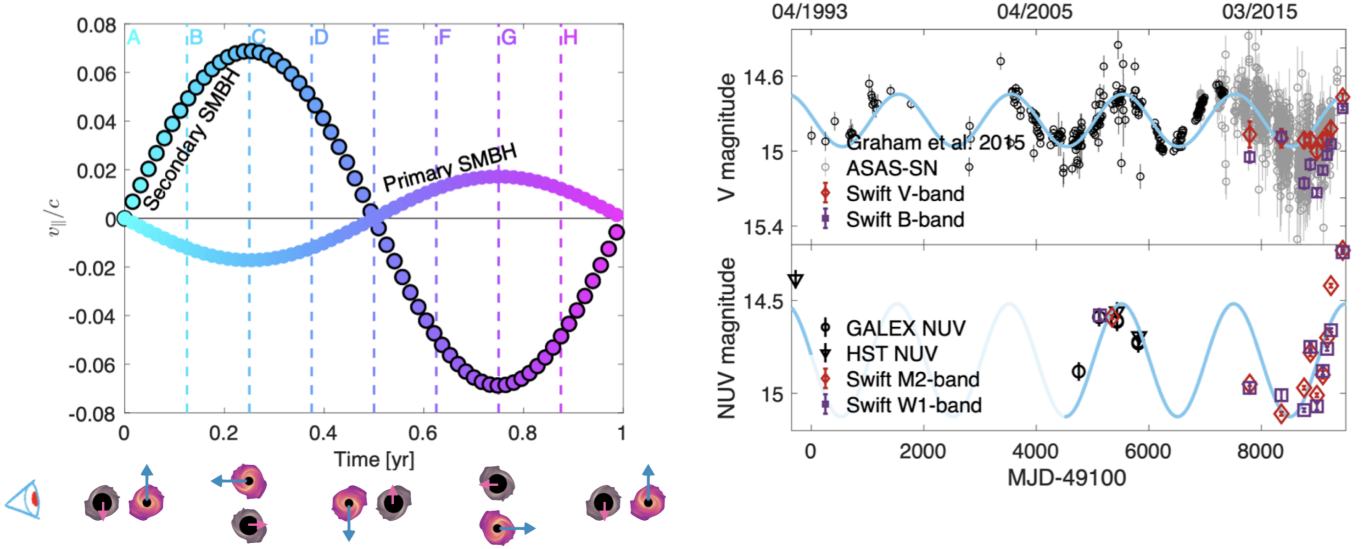


Figure 6. *Left:* Line-of-sight velocity for the primary and secondary SMBH in a binary with total mass $M = 10^9 M_{\odot}$, mass ratio $q = 1/4$, period $P = 1$ yr and inclination $I = 60^{\circ}$. The orientation of the binary with respect to the observer at various phases of the orbit is shown at the bottom of this figure. We have highlighted the mini-disk of the secondary SMBH, since it is typically more luminous and moves faster, and thus dominates the variability. Adapted from Charisi et al. (2022). *Right:* The optical (top) and UV (bottom) lightcurve of PG 1302-102. The blue lines show the Doppler model given the optical and UV spectral indices. From Xin et al. (2020b).

Beyond motivating the observability of the orbital Doppler boost, Eq. (13) offers a first consistency check for vetting this scenario. The photometric lightcurve of a periodic candidate provides the amplitude A_{ν} and period P , while a spectrum of the source provides the spectral index α_{ν} . An independent measurement of the total binary mass can often be obtained (though with large uncertainty) from the broad emission lines (Shen et al. 2008) or galaxy scaling relations (Peterson 2014; Shen et al. 2015). A combination of P and M give β_{orb} up to the mass ratio, and so the left and right-hand sides of Eq. (13) are specified up to the binary mass ratio and inclination. Hence, an observed periodic lightcurve with a central mass measurement and spectrum can be used to rule out the Doppler hypothesis, or constrain the range of viable mass ratios and binary inclinations (D’Orazio et al. 2015b; Charisi et al. 2018).

A more powerful consistency check comes with lightcurves in more than one observing band, *e.g.*, centered at ν_1 and ν_2 . By Eq. (12), both lightcurves will have the same shape and period, but their modulation amplitudes are related by (D’Orazio et al. 2015b),

$$\frac{A_{\nu_1}}{A_{\nu_2}} = \frac{(3 - \alpha_{\nu_1})}{(3 - \alpha_{\nu_2})}. \quad (14)$$

Hence, lightcurves and spectra in two observing bands provide a parameterless consistency check for the Doppler boost model. This multi-wavelength Doppler boost test was successfully carried out in the optical and UV to describe the sinusoidal oscillations in the quasar PG 1302 (Graham et al. 2015a; D’Orazio et al. 2015b; Xin et al. 2020b), which is currently still being monitored to determine if the periodicity is persistent and preferred to quasar noise (Liu et al. 2018a; Zhu & Thrane 2020). In the right panel of Figure 6, we show the multi-wavelength lightcurve of PG 1302 along with the Doppler boost model fit. The multi-wavelength Doppler signature was subsequently tested in 68 binary candidates from Graham et al. (2015b); Charisi et al. (2016) with optical and UV lightcurves finding that $\sim 1/3$ are consistent with the model prediction (Charisi et al. 2018). However, because quasars have wavelength-dependent variability (Xin et al. 2020a), the signature can also be observed by chance in a control sample of non-periodic quasars at a rate of 20 – 40%, depending on the quality of the data (Charisi et al. 2018). Therefore, it is challenging to distinguish this signature from intrinsic quasar variability, especially if the available multi-wavelength data are sparse.

Note that if the source consists of not one isotropically emitting blob (*e.g.*, the mini-disk bound to one of the SMBHs in the above derivation), but many such blobs moving with line-of sight speed $\beta \cdot \hat{\mathbf{n}}$, then we must sum the specific intensity per unit length along the line of blobs, introducing an extra factor of D from the isotropic case. This latter situation could describe a jet, for example. Conceptually, the line of emitting blobs is length contracted along the direction of motion, decreasing the flux by a factor of D ,

$$F_{\nu}^{\text{jet}} = D^{2-\alpha_{\nu}} F_{\nu}^{\text{jet}'}, \quad (15)$$

where the time-dependent line-of-sight velocity will also be different from the single blob (disk case). If we assume that the line of emitting blobs is indeed a jet attached to one of the binary components, then the first-order effect is for the binary orbital motion to change the jet to line-of-sight angle, causing periodic brightness modulations with a different amplitude than in the disk case. This distinction could help discern variability with a jet origin from that with a disk origin. O'Neill et al. (2022) use the jet-Doppler model to explain the variability of the binary candidate PKS 2131-021 (Ren et al. 2021).

Finally, for demonstrative purposes, we above assumed a circular orbit and that all of the light came from the secondary SMBH. Both of these assumptions can be relaxed resulting in a deviation of the lightcurve from a sinusoid (Hu et al. 2020; Charisi et al. 2022). Deviations from sinusoidal variability can also occur if the intrinsic source luminosity is not constant (Charisi et al. 2022). Note that here, we also did not include percent-level effects due to finite-light travel time (Rømer delay), or general relativistic pericenter precession, which can become important for highly eccentric orbits. All such terms can in principle be added to the Doppler model.

Binary Self-Lensing

If the binary is inclined sufficiently close to the line-of-sight, then the light from the accretion disk around one SMBH will be lensed once per orbit by the other SMBH in the binary. The characteristic scales of the problem relevant for lensing are (1) the Einstein angle at conjunction,

$$\theta_E = \sqrt{\frac{2R_{Sl}a}{D_A^2}}, \quad (16)$$

for Schwarzschild radius of the lens $R_{Sl} \equiv 2GM_{\text{lns}}/c^2$ with M_{lns} the mass of the lensing SMBH, (2) the binary angular scale, $\theta_{\text{bin}} \equiv a/D_A$, for a binary with orbital separation a at angular diameter distance D_A and, (3) a minimum size scale of emission at a given wavelength, $\theta_{\text{min}} \equiv 6GM_{\text{src}}/(D_A c^2)$, approximated here by the innermost stable circular orbit (ISCO) of the SMBH which is being lensed, with mass M_{src} . With these scales, we follow D'Orazio & Di Stefano (2018); D'Orazio & Di Stefano (2020); D'Orazio & Loeb (2020) to derive the probability for a significant lensing event. Assuming that we observe the binary for at least one orbit, the probability is found from counting all ring orientations on the sphere for which the source passes within the Einstein radius of the lens at conjunction. The result approximates to

$$\mathcal{P} \approx \frac{\theta_E}{\theta_{\text{bin}}} = \sqrt{\frac{2R_{Sl}}{a}} \approx 0.1 \left(\frac{a}{200R_{Sl}} \right)^{-1/2}. \quad (17)$$

The duration of the lensing flare will be

$$\mathcal{T} \approx \frac{\theta_E}{\theta_{\text{bin}}} P = \mathcal{P} P \approx 0.03 \text{yr} \left(\frac{1+q}{2} \right)^{-3/2} \left(\frac{a}{200R_{Sl}} \right) \left(\frac{M}{10^8 M_{\odot}} \right), \quad (18)$$

which is one tenth the duration of the orbit in this example.

The magnification of a point source by a point mass lens is,

$$\mathcal{M} = \frac{u^2 + 2}{u\sqrt{u^2 + 4}}, \quad (19)$$

where u is the sky-projected separation between source and lens in units of θ_E . A significant lensing event is defined to occur at $u = 1$, where $\mathcal{M} \approx 1.34$. For close encounters of the projected point-source and lens positions, $u \ll 1$, and the magnification limits to $\mathcal{M} \rightarrow 1/u$. Hence the maximum magnification can be estimated as $1/u_{\text{min}} = \theta_E/\theta_{\text{min}}$,

$$\mathcal{M}_{\text{max}} \approx \frac{\theta_E}{\theta_{\text{min}}} \approx \sqrt{\frac{2}{9}} \frac{1}{q^2} \frac{a}{R_{Sl}} \approx \frac{20}{3} q^{-1} \left(\frac{a}{200R_{Sl}} \right)^{1/2}, \quad (20)$$

reaching a magnification of 10 for $q = 2/3$.

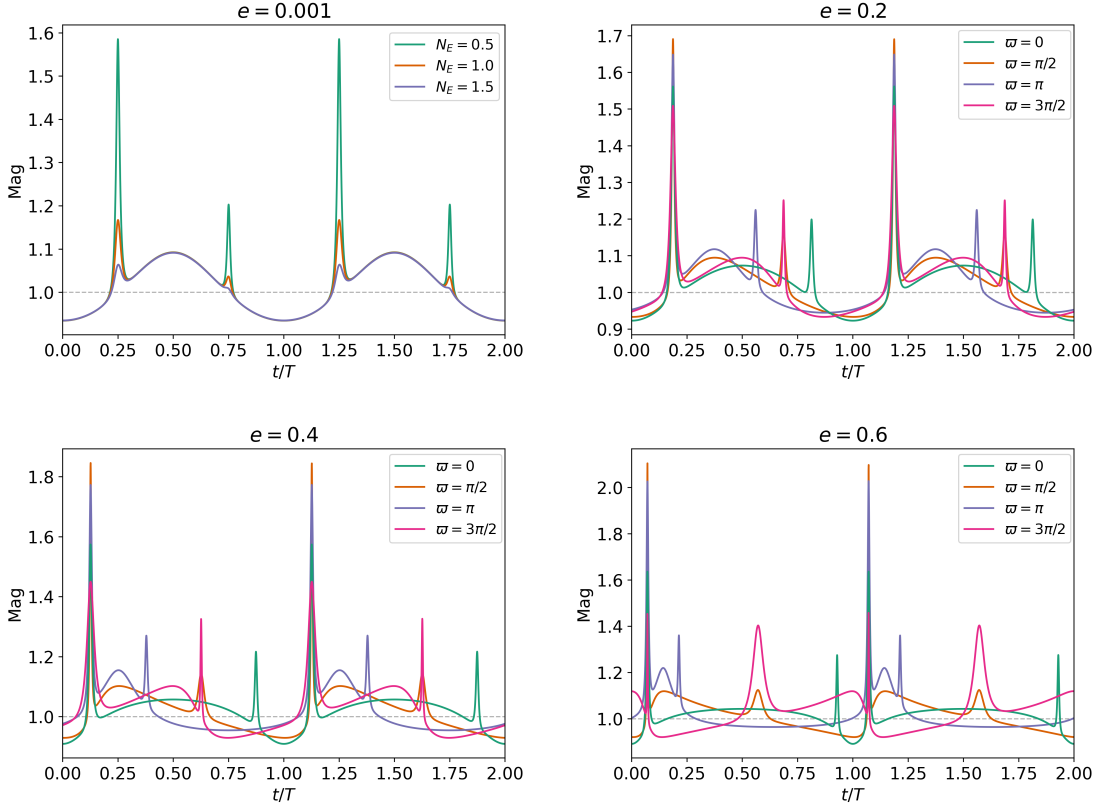


Figure 7. Example Doppler+lensing lightcurves with parameters detailed in the text. The *top left panel* shows the change in lightcurve with inclination, for inclinations that cause a $N_E = 0.5\times, 1.0\times,$ and $1.5\times$ Einstein separation of source and lens at conjunction. The remaining panels show how the Doppler+lensing signature changes for eccentric orbits with different eccentricities and arguments of pericenter ϖ .

Lightcurves of a steadily accreting source viewed at an angle where both Doppler boosting and lensing are prominent is shown in Figure 7. The lensing signature is unique; for a circular orbit (top left panel) it manifests as a symmetric flare occurring at the flux average of the sinusoidal Doppler modulation – for eccentric orbits, the symmetric flares persist, but occur with a different relative magnitude and width at different (predictable) phases of a non-sinusoidal Doppler oscillation. The top right and bottom panels of Figure 7 show how the lightcurve changes with eccentricity e and argument of pericenter ϖ .⁷ Note that for eccentric orbits, the orbit can experience pericenter precession and the timing of the lensing flares would drift. This precession could be due to general relativity or sufficient amounts of surrounding matter.

In the case of a point source, this flare will be achromatic. When the emission region size is of order the Einstein radius or larger, finite-source-size effects cause the shape and magnification to become wavelength dependent. Specifically, the shape and magnification of the lightcurve will depend on the shape and size of the emitting region at a given wavelength. Examples and specific criteria for a steady-state accretion disk source are given in D’Orazio & Di Stefano (2018). In more extreme situations, finite lensing could even probe horizon scale features of the accretion flow around the source SMBH (Davelaar & Haiman 2022a,b). In addition to repeating lensing flares, matter in the accreting binary may also cause eclipses (Ingram et al. 2021).

The best candidate for such a Doppler plus self-lensing SMBHB derives from the Kepler light-curve for the “Spikey” system, which is remarkably well fit by an eccentric SMBHB Doppler+lensing model (Hu et al. 2020), albeit for only one flare on top of a sawtooth-shaped modulation. From observations of one putative lensing flare, however, an orbital period can be inferred allowing predictions for future flares and so a test of the SMBHB model, which could rule out or provide convincing evidence for a milli-parsec separation SMBHB (D’Orazio et al. *In prep.*).

⁷ The model has ten parameters. In addition to the specified values of e and ϖ , the parameters chosen for Figure 7 are $M = 10^9 M_\odot$, $q = 0.3$, $P = 5$ yrs, $\alpha_\nu = -2$, $f_L = 0.5$, $N_E = 0.5$, $v_z = 0$, $t_0 = 0$, where f_L is the ratio of light coming from the secondary compared to the primary, v_z is the barycenter velocity of the source in the line-of-sight direction, and t_0 is the starting epoch. For these parameters $N_E = 0.5$ corresponds to a binary inclination of $I = 87.08^\circ$.

3.4.3. Reverberation

The above considers hydrodynamic, Doppler, and self-lensing sources of periodic variability in directly observed continuum emission. A more complete description must place this emission in the broader context of AGN. Specifically, the medium surrounding the central AGN power source can reprocess this emission via absorption and scattering processes. As we saw in §3.3.1, broad-line reprocessing is one example of such reverberation of the central continuum emission.

Beyond the broad line region, optical to UV radiation can be absorbed by surrounding dust structures. This results in an echoed infrared (IR) continuum with the same periodicity as the optical/UV, but with a time delay and a diminished amplitude of variability. While any optical/UV continuum variations can be echoed by dust, D’Orazio & Haiman (2017) predict time delays and variability amplitude ratios between IR and optical/UV lightcurves that differ for reverberation of spatially isotropic illumination (*e.g.*, periodic accretion variability of §3.4.1) vs. anisotropic illumination via the Doppler Boost (see Figure 8). Three main differences in particular are: (1) periodically variable IR lightcurves caused by the Doppler boost have an extra quarter cycle phase lag compared to the isotropic reverberation case, for the same reverberating dust structure. (2) In the limit of small light travel time across the dust structure compared to the variability period, isotropically illuminated dust structures echo a maximum variability amplitude equal to the continuum level, whereas the echoed Doppler boosted variability amplitude drops to zero, completely washing out the IR signal (see Figure 3 of D’Orazio & Haiman 2017). Finally, (3) dust illumination by Doppler boosted emission allows for a new possibility of “orphan IR periodicity”; for example, a near face-on binary does not produce any Doppler boosted optical/UV periodicity, since the line-of-sight velocity is small, but dust at different inclinations to the binary plane than the observer does see the anisotropic, time variable Doppler boosted illumination. Hence, constant continuum UV/optical emission would be accompanied by periodic variability in the echoed IR emission. This signature is yet to be observed. Using WISE IR data, Jun *et al.* (2015); D’Orazio & Haiman (2017) utilize these IR echo models to further vet the Doppler-boost hypothesis for the SMBHB candidate PG 1302 (see Figure 8).

Scattering of the direct continuum emission from each accreting SMBH in the binary could lead to a time-changing polarization degree and polarization angle of the observed emission. Dotti *et al.* (2022) consider scattering of light emitted from one of the binary components by a surrounding circumbinary ring. For fraction s of light scattered by the ring, Dotti *et al.* (2022) predict $0.2s$ -level periodic variability in the polarization degree, modulated at the binary orbital period, with minimum polarization degree coincident with the maximum of the continuum flux. Periodic variability in the polarization angle occurs at the $1\times$ or $2\times$ the binary orbital period with typical amplitude of variation at the 1° level. Both are at the limits of detection via modern polarimetry of AGN (see Dotti *et al.* 2022, and references therein).

While each of the above reprocessing phenomena occur also for continuum emission from a single SMBH, the time changing distance from the binary to the reprocessing region caused by orbital motion, as well as temporal, and sometimes spatial, anisotropic illumination could imprint identifiable features on the reprocessed emission. Hence, these reprocessed signatures offer an extra handle on distinguishing the causes of periodic variability of AGN lightcurves and so for testing the SMBHB hypothesis.

3.4.4. Periodicity Searches and Sources of Noise and Confusion

The search for quasars with periodic variability has seen rapid developments in the last few years due to the advent of time-domain surveys, which systematically scan the sky and record the brightness evolution for millions of sources. These surveys have provided large samples of quasar lightcurves and allowed for the first systematic searches, which have returned ~ 250 SMBHB candidates.

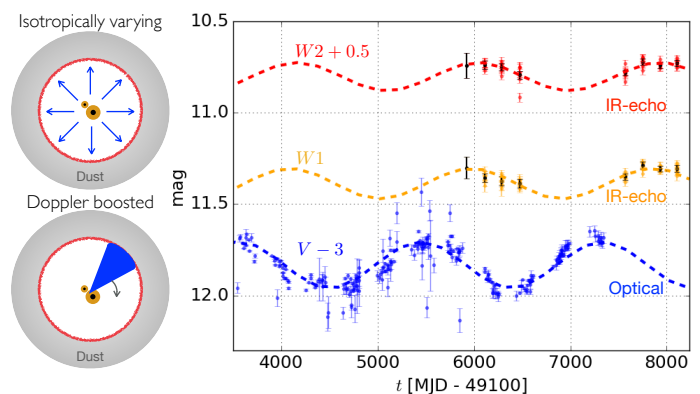


Figure 8. *Left:* Schematics representing dust tori (grey) illuminated by optical/UV emission (blue) from a central accreting binary, thereby heating the dust (red rings) causing it to echo the continuum emission in infrared emission. Isotropically varying and Doppler boosted emission will illuminate the dust differently resulting in different echoed IR emission (§3.4.3). *Right:* Optical (V-band, blue) and IR (WISE W1- and W2-bands, orange and red) emission from SMBHB Doppler boost candidate PG 1302-102 showing phase-lagged and diminished amplitude variability in the IR (Jun *et al.* 2015; D’Orazio & Haiman 2017), dashed lines are sinusoidal fits.

More specifically, [Graham et al. \(2015b\)](#) analyzed a sample $\sim 245,000$ quasars from the Catalina Real-time Transient Survey (CRTS) and identified significant evidence for periodicity in 111 quasars. [Charisi et al. \(2016\)](#) performed a systematic search in a sample of $\sim 35,000$ quasars from the Palomar Transient Factory (PTF) and detected 33 candidates. One additional candidate was found in a small sample of 9000 quasars from the Panoramic Survey Telescope and Rapid Response System Medium Deep survey (Pan-STARRS MDS; [Liu et al. 2019](#)), while five more candidates were discovered in an even smaller sample of 625 AGN from the Dark Energy Survey (DES; [Chen et al. 2020](#)). A larger sample of 123 candidates was detected recently from the analysis of a sample of 143,700 quasars from the Zwicky Transient Facility (ZTF; [Chen et al. 2022b](#)).

The above candidates have periods from a few hundred days to a few years, with separations ranging from a few to a few hundred milli-parsecs. The magenta dots ([Graham et al. 2015b](#)), orange x's ([Charisi et al. 2016](#)), black x ([Liu et al. 2019](#)), black +'s ([Chen et al. 2020](#)), and chartreuse stars ([Chen et al. 2022b](#)) in Figure 1 denote photometric variability candidates from CRTS, PTF, Pan-STARRS MDS, DES and ZTF surveys, respectively. The range of searched (and thus detected) periods is dictated by the data. The baseline of the lightcurve (i.e. the maximum interval of observations) determines the maximum period, with most searches requiring that at least 1.5 cycles of periodicity are present within the available baseline. The minimum allowed period is determined by the survey cadence, i.e. how often observations are taken, but most studies have limited the searches to periods of more than a month to avoid unmodeled photometric effects mainly from the lunar cycle. It is also worth pointing out that even though the above studies employed distinct search methods, the rate of periodicity detection is within an order of magnitude, i.e., $10^{-3} - 10^{-4}$.

Identifying periodicity in quasars is extremely challenging and the above samples likely contain a large number of false detections. The main reason is that quasars have stochastic variability which can both mimic periodicity, introducing false positives, and hinder the detection of real periodic signals ([Vaughan et al. 2016](#); [Witt et al. 2022](#)). This effect is pronounced for relatively long periods for which we cannot observe many cycles within the available baselines. We emphasize that despite the common misconception that the above samples of periodic candidates contain false positives because the stochasticity of the noise was not included in the statistical analysis, all of the above systematic searches assumed that the quasar noise is described by a Damped Random Walk (DRW) model, which is currently the most successful description of quasar variability ([MacLeod et al. 2010](#); [Kozłowski et al. 2010](#)). In particular, [Graham et al. \(2015b\)](#) used a combination of wavelets and auto-correlation function to select periodic candidates. Then for each observed lightcurve, they simulated a DRW lightcurve with properties like the observed lightcurve (sampling, gaps, photometric errors) and showed that the mock population cannot produce candidates that pass the periodicity detection threshold. [Charisi et al. \(2016\)](#) used the Lomb-Scargle periodogram to select quasars with periodic variability, and assessed the periodicity significance with DRW simulations. For each lightcurve, they fit a DRW model and subsequently simulated 250,000 mock lightcurves with the best fit DRW parameters and properties like the observed to account for trial factors from searching in a large sample and over multiple frequency bins. They assessed a false alarm probability for each source by comparing the periodogram peak of the observed lightcurve with the distribution of peaks from the simulations. [Chen et al. \(2020\)](#) followed a very similar approach to [Charisi et al. \(2016\)](#), but generated 50,000 mock lightcurves for each observed lightcurve, since the search sample was smaller. [Liu et al. \(2019\)](#) pre-selected periodic candidates using the Lomb-Scargle periodogram under the assumption of white noise and down-selected candidates by performing a maximum likelihood selection between a DRW and a DRW+periodic model. Finally, [Chen et al. \(2022b\)](#) followed a similar approach to [Liu et al. \(2019\)](#).

[Sesana et al. \(2018\)](#) also demonstrated that not all candidates can be genuine binaries by extrapolating the population of binaries given the candidates identified in the CRTS ([Graham et al. 2015b](#)) and PTF ([Charisi et al. 2016](#)) samples. They concluded that the expected GW background from the inferred population is in moderate tension with upper limits from PTAs, which further indicates that the samples contain false positives. Using similar population arguments, [Holgado et al. \(2018\)](#) estimated the maximum fraction of blazars (a sub-class of quasars in which the relativistic jet is pointed towards our line-of-sight) that can be associated with short-period binaries and suggested that the binary scenario is not a good interpretation for the year-long quasi-periodicities observed in blazars.

Given the contamination with false detections, follow-up efforts have focused on collecting multi-wavelength data in order to find converging evidence that could signify the presence of a binary in candidate quasars, covering the entire array of potential signatures described above, such as (1) variability in the broad emission lines (§3.3.1; [Song et al. 2021](#); [Ji et al. 2021a](#); [Nguyen et al. 2020](#)) (2) spectral X-ray signatures (§3.3.2; [Saade et al. 2020](#)), (3) periodicity with multiple periodic components and a characteristic frequency pattern (§3.4.1; [D’Orazio et al. 2015a](#); [Charisi et al. 2015](#)), (4) multi-wavelength Doppler boost or self-lensing (§3.4.2; [D’Orazio et al. 2015b](#); [Charisi et al. 2018](#); [Xin et al. 2020b](#)), (5) the IR dust reverberation signature (§3.4.3; [Jun et al. 2015](#); [D’Orazio & Haiman 2017](#)), and (6) the imprint of binaries on radio jets (§3.5; [Kun et al. 2015](#); [Mohan et al. 2016](#); [Qian et al. 2018](#)). A subset of the candidates show one or more of the above promising signatures and warrant further monitoring. However, not all of these signatures are unique to binaries, nor is it always clear when multiple effects should occur at the same

time, and thus they cannot be easily distinguished from the intrinsic variability of typical single-SMBH quasars *e.g.*, Charisi et al. (2018).

As is apparent from the above, the optical band dominates the discovery space in time-domain searches, due to the abundance of photometric data produced from ground-based surveys primarily during the last decade. Time-domain surveys have operated across the electromagnetic spectrum for a while (*e.g.*, UV/GALEX; Martin et al. 2005, mid-IR/NEOWISE; Mainzer et al. 2014, X-rays/Swift; Roming et al. 2005, eROSITA; Predehl et al. 2021, gamma-rays/Fermi LAT; Atwood et al. 2009), but these surveys typically do not have the required combination of data quantity (as mentioned in §3.1, SMBHBs are relatively rare and thus a large sample of quasars is necessary) and data quality (long baselines, with dense enough sampling) to allow for similar systematic searches. One exemption is the Swift BAT survey spanning 105 months, in which two independent systematic searches in a small sample of <1000 AGN have returned one additional candidate (Serafinelli et al. 2020; Liu et al. 2020). This rate is roughly consistent with the optical searches above.

Beyond the systematic searches, there have been multiple reports of serendipitous detections of quasar periodicity in multiple bands. In §5.2, we present a likely incomplete summary of these candidates.

Pros and Cons: Periodic Lightcurves

Pros:

- The expectation for periodic brightness modulation in binaries is simple and intuitive – the two body problem is periodic. Many mechanisms can produce periodicity, as shown in a variety of analytical and numerical studies.
- Some signatures (*e.g.*, the relativistic Doppler boost) are unique containing testable multi-wavelength predictions and possible reverberation signatures.
- This method has been applied in large samples of AGN from past or ongoing time-domain surveys revealing hundreds of promising candidates.
- Upcoming time-domain surveys like LSST will provide even bigger samples, which are required for the detection of rare short-period binaries.

Cons:

- AGN variability is stochastic and can mimic periodicity. Therefore, the samples of candidates are likely contaminated with false detections.
- Not all signatures are unique, making them hard to distinguish from typical quasar variability, especially in the limit of sparse data.
- Building confidence in the candidates requires observations of many cycles of periodicity, which for periodicities of a few years requires time (decades).
- The multi-wavelength Doppler boost test requires spectra and multi-epoch photometry in two observing bands, while lensing requires relatively high cadence over long temporal baselines.
- Application of IR reverberation models require high-cadence IR all-sky surveys (*e.g.*, to build a large sample and systematically search for binaries) or long-term follow-up of individual candidates.
- Polarization signatures are at the limit of detection and can be confused by scattering from intervening gas in the AGN host galaxy.
- Models of binary accretion are still young.

3.5. Jet Morphology

Searching for peculiar or spatially periodic features in AGN jets was one of the first methods proposed for finding SMBHBs (Begelman et al. 1980). The idea is that accretion onto the binary may result in a jet launched from one or both SMBHBs. The binary orbit (or the binary coalescence) can be imprinted on the large-scale features of the jet (see left panel of Figure 9).

3.5.1. Periodic Wiggles and Helicity

In one set of models, shocks at the jet base launch plasmoids that travel away from the central power source at relativistic velocities on ballistic trajectories. If the jet power source is stationary, these plasmoids will trace out a line in space, resulting in a straight collimated jet (Rees 1978). If the jet is precessing, the plasmoids will trace out a conical helix, whereas if the base of the jet is moving, *e.g.*, due to the orbital motion in a binary system, the shape of the jet depends on the orientation of the jet axis

with respect to the binary orbital plane, with the plasmoids tracing a cylindrical/conical helix if the jet axis is perpendicular/titled with respect to the orbital plane (Rieger 2004).

The theory describing the projected shapes of precessing jets was first laid out in Gower et al. (1982). In a precessing jet, the opening angle, Ψ , is given by the amplitude of the precession angle, while the wiggle wavelength is set by the precession period and sky projection. Jet precession can be observed both in a single-SMBH AGN and in a binary system. For a single SMBH, precession can be caused by Lense-Thirring precession of a disk misaligned with the SMBH spin (see Liska et al. 2018, and refernces therein). In a binary, precession could be caused by geodetic precession of the SMBH spin which is misaligned with the binary orbital angular momentum (Begelman et al. 1980; Roos 1988), or torquing of a disk around the jet-launching SMBH, which is misaligned with the binary orbital plane. The former occurs on long timescales, upwards of thousands of years,

$$P_{\text{geop}} \approx 9 \times 10^3 \text{yr} \, q^{-1} \left(\frac{a}{10^{-2} \text{pc}} \right)^{5/2} \left(\frac{M}{10^8 M_{\odot}} \right)^{-3/2}. \quad (21)$$

However, if the disk is torqued by a binary companion at distance a , then the precession timescale, P_{prc} , of a disk around the secondary (primary), perturbed by the primary (secondary) is significantly shorter (Lai 2014),

$$\frac{P_{\text{prc}}}{P_{\text{orb}}} = -\frac{8}{3} \frac{1 + q^s}{\sqrt{1 + q^{-s}}} \left(\frac{a}{r_d} \right)^{3/2} (\cos \chi)^{-1}, \quad (22)$$

where $s = 1$ ($s = -1$) corresponds to the secondary (primary) disk perturbed by the primary (secondary), χ is the angle between the disk angular momentum and the binary orbital angular momentum, r_d is the outer radius of the precessing disk. This calculation also assumes that the disk surface density falls as $1/r$.

Even if neither of the above precession mechanisms operate, the binary orbital velocity can generate a similar effect. If the jet launching SMBH has an orbital velocity due to its motion in a binary system, then the plasmoids are launched with direction and speed given by relativistic velocity addition of the jet velocity, \mathbf{v}_{jet} , and the orbital velocity of the base of the jet, \mathbf{v}_{orb} . Hence, the jet launching velocity is modulated in direction and magnitude due the course of an orbit. This also results in plasmoids tracing a cone (or a cylinder) with opening angle given by $\Psi \approx v_{\text{orb}}/v_{\text{tot}} \cos \chi$ (Roos et al. 1993), but now the wiggle wavelengths are set by the orbital period.

It is important to note that the observed and source frame precession periods can be very different in the case of large jet velocities directed near to the line of sight. For jet velocity $\beta_j \equiv v_j/c$, time-dependent angle to the line of sight $\phi_j(t)$, and duration in source frame of $(t_{\text{src}} - t_0)$ the observer and source frame times are related by,

$$\Delta t_{\text{obs}} = (1 + z) \int_{t_0}^{t_{\text{src}}} [1 - \beta_j \cos \phi_j(t')] dt' \quad (23)$$

(e.g., Roland et al. 2008; Caproni et al. 2013). For example, the observer- and source-frame jet-precession periods measured for BL Lacertae (2200+420; Caproni et al. 2013) are 12.11 yr and 550 yr, respectively (translating to an inferred source-frame binary orbital period of 335 yr in that model). For the candidate in PKS 1830-211, they are 1.08 yr and 30.8 yr, respectively (§5.3; Nair et al. 2005). This has the benefit of probing much longer orbital periods than available through photometric periodicity (§3.4.4).

Varying the viewing angle for either precession or orbital modulation models results in a zoo of possible observed jet shapes, which encode the periodic nature of the jet launching. In addition to the projected positions of jet plasmoids on the sky tracing out the jet shape, the above described ballistic models also predict the apparent velocity of each plasmoid and its Doppler factor. Fitting a jet model to the data requires tracking the apparent velocity and sky position of multiple plasmoids over time, in order to constrain the evolution of jet motion and disentangle the variety of parameters in the model (e.g., see right panels of Figure 9).

Further modeling has included the impact on the jet morphology from the possible orbital decay due to GWs (Kulkarni & Loeb 2016), the possibility of emission from double (and possibly intersecting) jets (Palenzuela et al. 2010; Gold et al. 2014a,b; Bright & Paschalidis 2023), and MHD simulations of a wobbling jet in an ambient medium, constraining jet precession angles for which successful propagation can occur (Fendt & Yardimci 2022).

Several candidates have been identified based on the above jet signatures. In §5.3, we present a (likely incomplete) summary of the main candidates. The inferred binary properties from these candidates are plotted in Figure 1 as yellow ‘pluses’ (we have only reported mean or typical inferred binary parameters and draw a down caret in the case of an upper limit). However, we emphasize that, like many of the aforementioned electromagnetic signatures of SMBHBs, jet wiggles are also not unique and may be produced by alternative mechanisms. For instance, instabilities such as the Kelvin-Helmholtz instability acting between the fast-moving jet material and its surroundings can produce distorted jets, mimicking the wiggles from a binary system (Lobanov &

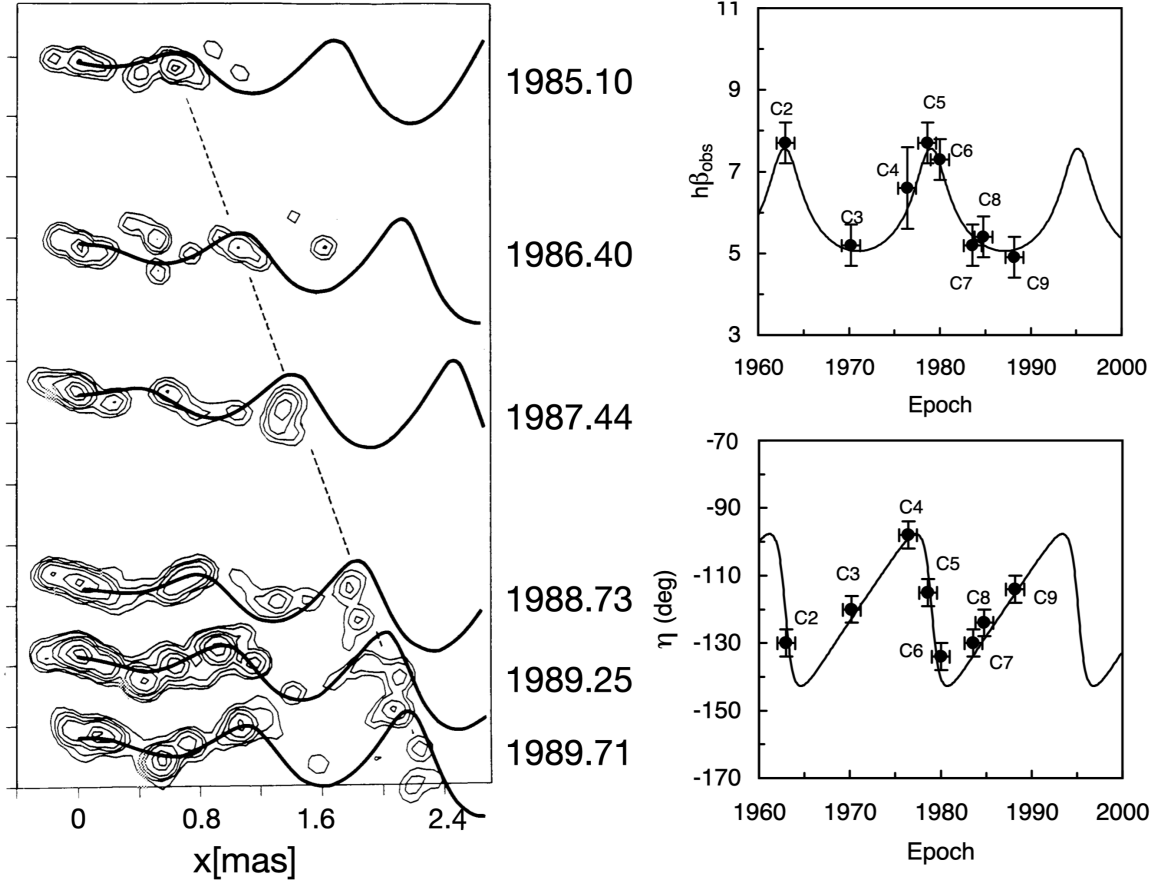


Figure 9. *Left:* Example radio contours of the jet in quasar 1928+738 exhibiting “wiggle” and overlaid jet+SMBHB model, from [Roos et al. \(1993\)](#). *Right:* Data for the positions of different jet components η and corresponding observed proper motions in units of the speed of light (up to Hubble parameter h), β_{obs} , for the jet in quasar 3C 273. The periodic nature, over the considered epochs, can be fit by a model where the jet is attached to one of the SMBHs in a binary, from [Abraham & Romero \(1999\)](#).

[Zensus 2001](#); [Zhao et al. 2011](#)). Long-term monitoring or higher-resolution imaging of the jets can help differentiate the possible scenarios.

Several studies have followed up candidates selected with a different method, e.g., quasars with periodic variability, to search for jet distortions. In some cases, these observations have found jet signatures consistent with the binary candidate properties and offer independent support for the binary nature of these sources. In §5.3.2, we briefly summarize these follow-up efforts and findings for the main candidates.

3.5.2. X’s and Other Shapes

Another class of SMBHB jet morphology models have been devised to explain the 5-10% of radio galaxies that exhibit peculiar “winged” or X-shaped radio structures ([Leahy & Williams 1984](#); [Yang et al. 2019](#)). Explanations relying on an SMBHB include mis-aligned jets attached to each SMBH in a binary or a merger-induced spin flip ([Merritt & Ekers 2002](#); [Gopal-Krishna et al. 2003](#)). There exist, however, a range of suggested causes that do not invoke SMBHBs (starting from [Rees 1978](#)), and including recent GRMHD simulations which show that a transient initial state in the jet launching process for a single SMBH can naturally generate X-shaped radio morphologies ([Lalakos et al. 2022](#)).

Pros and Cons: Jet Morphology

Pros:

- Many jets with wiggles and “wing-” or X-shapes have been observed resulting in many proposed binary candidates.
- The periodic jet structures can sometimes probe long (~ 100 yr) orbital periods due to strong relativistic effects.
- Could learn from prototypical systems: galaxy 3C 75 with two jets, (but separation of SMBHs is large, [Owen et al. 1985](#)), or stellar-mass (micro-quasar) system with remarkable jet morphology, SS433 (see [Blundell et al. 2018](#), and references therein).

Cons:

- These jet signatures are indirect and not unique and thus they can be confused with jet features generated by a single SMBH.
- Only $\sim 10\%$ of AGN are radio loud.

3.6. Direct Imaging and Orbital Tracking at Sub-Parsec Separations

Until now we have only considered indirect means for detecting sub-parsec separation SMBHBs. The reason, as discussed in §3.1, is the small angular diameter of the binary separation on the sky (Eq. 9), of order $10\mu\text{as}$ or smaller.

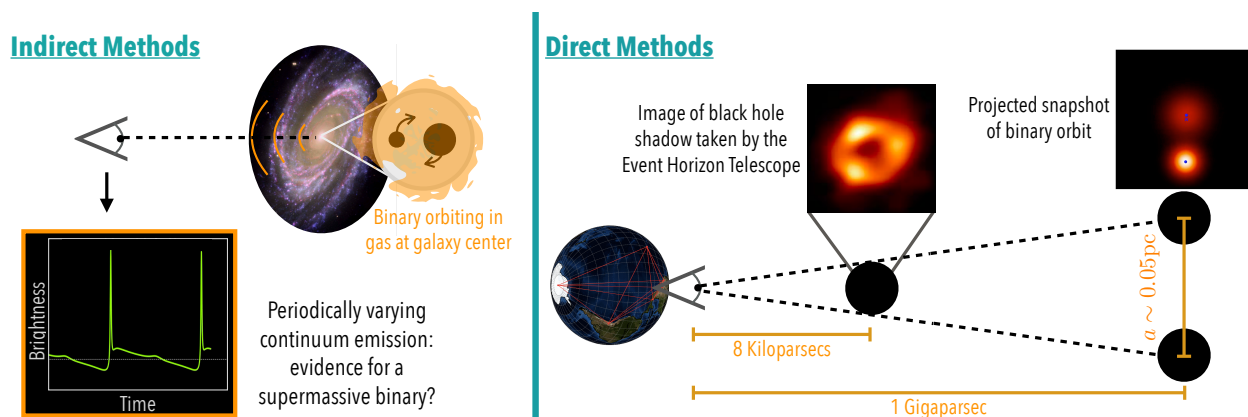


Figure 10. General classes of methods for electromagnetic identification of SMBHBs at sub-parsec separations. *Left:* Due to the small angular scales of SMBHBs, indirect methods for their detection are most often employed (§’s 3.3-3.5) *Right:* Only the most extreme resolving power available via, e.g., mm-wavelength VLBI, could access the required spatial scales. Gaps in our knowledge of mm-wavelength emission from SMBHBs and uncertainty in the binary population remain obstacles towards direct tracking of sub-parsec separation SMBHB orbits.

Millimeter-wavelength Very Long Baseline Interferometry (mm-VLBI) can achieve $\sim 10\mu\text{as}$ resolution, as evidenced by the Event Horizon Telescope, which imaged the accretion flow on horizon scales around M87 ([Event Horizon Telescope Collaboration et al. 2019](#)) and Sgr A* ([Event Horizon Telescope Collaboration et al. 2022](#)). As illustrated in Figure 10, the angular scale of the horizon of the Milky Way SMBH (Sgr A*) is approximately the same as the angular scale of an SMBHB orbit with 0.05 pc separation at a Gpc ($\sim 10\mu\text{as}$). Furthermore, such a system would have an orbital period of less than 20 years for total binary masses $M \geq 3 \times 10^9 M_\odot$. For a system at 500 Mpc ($z \approx 0.14$), $10\mu\text{as}$ corresponds to a binary separation of ≈ 0.024 pc for which the binary would have an orbital period less than 20 years for total binary masses $M \geq 3 \times 10^8 M_\odot$. Using a simple gas and GW-driven binary population model, limited by GWB upper limits from PTAs, and tied to the radio-loud quasar luminosity function (see §2.2), [D’Orazio & Loeb \(2018\)](#) estimate that a few to ~ 100 of such resolvable systems are bright enough, have short enough orbital period, and large enough angular scale to track with EHT-like observations, though model uncertainties are large.

VLBI is not amenable to surveys, tracking of binary orbits would require monitoring target binary candidates identified through other means discussed above, or by GW observations with PTAs ([D’Orazio & Loeb 2018](#)), if the host galaxy can be pinpointed within the large GW error volumes ([Goldstein et al. 2018, 2019](#)). Assuming the binary appears as two point sources on the sky, each observation would require clusters of observations at different baseline orientations with respect to the line joining the

point sources. In order to confirm the orbital motion, and therefore strong evidence for binarity, these clusters of observations would need to be repeated over the span of an orbital period. Hence, high probability candidate systems that are bright at mm-wavelengths are required. Additionally, further modeling of the mm-emission region surrounding accreting SMBHBs and modeling of the interferometric signature is required to make further progress.

We note that the SMBHB model for the repeating flares in quasar OJ 287 posits an apocenter binary separation of $27\mu\text{as}$. This in addition to OJ 287 being one of the brightest mm-wavelength sources on the sky make it a prime candidate for such monitoring with mm-VLBI. It is, however, unlikely that mm-wavelength emission is coming from both the secondary and the primary, as opposed to emanating from the base of the jet around the primary (Komossa et al. 2023b). Hence, even when resolved, evidence for the binary hypothesis may be sparse, and requires a more sophisticated accretion model to interpret.

In addition to mm-VLBI, near IR, optical interferometry with GRAVITY+ could resolve illuminated broad-line or dusty regions around sub-parsec separation SMBHBs (Dexter et al. 2020). Another exciting prospect is the possibility of μas -level astrometry for nearby SMBHBs with the ngVLA (Wrobel & Lazio 2021, 2022) or *Gaia* (D’Orazio & Loeb 2019, though the number of expected targets is marginal) to vet SMBHB candidates.

Pros and Cons: Direct, Sub-pc Orbital Tracking

Pros:

- Would deliver direct evidence for a sub-pc separation SMBHB on orbital timescales.

Cons:

- Requires high probability target systems and expensive, multi-epoch VLBI (or GRAVITY+ interferometric) observations and thus would only be possible for a limited number of targets.
- Models for emission at wavelengths where imaging or astrometric tracking is possible are still under development.

3.7. Gravitational Waves and Multi-Messenger Constraints

While we have focused on electromagnetic signatures of SMBHBs, GW observations will provide a definitive handle on the population near merger, providing a boundary condition for a continuity-equation description of the population (§2.2). The main classes of GW observatories that will observe SMBHBs are:

- **Space-borne interferometers** such as the Laser Interferometer Space Antenna (LISA; Amaro-Seoane et al. 2017) or Tian-Qin (Luo et al. 2016) will observe in the millihertz (mHz) frequency band, $f_{\text{GW}} \approx 10^{-4} - 10^{-1}$ Hz, and capture the mergers of $\approx 10^5 - 10^7 M_{\odot}$ SMBHBs out to redshifts of $z \sim 20$ (see Figure 11 and Amaro-Seoane et al. 2023). SMBHB population models place the expected LISA merger rate between of order one to several hundred per year (see below).
- **Pulsar Timing Arrays (PTAs)** are sensitive to GWs in the nanohertz frequency band, $f_{\text{GW}} \approx 10^{-9} - 10^{-7}$ Hz, emitted during the late inspiral the most massive $\approx 10^8 - 10^{10} M_{\odot}$ SMBHBs. PTAs have recently detected evidence for a GW background (Agazie et al. 2023c; EPTA Collaboration et al. 2023; Reardon et al. 2023; Xu et al. 2023), likely produced by binaries across the universe, but dominated by SMBHBs with $z < 1$ and mass $\gtrsim 10^9 M_{\odot}$ (Agazie et al. 2023b; Antoniadis et al. 2023b). Individual SMBHBs in the relatively nearby universe, $z \lesssim 0.5$ are expected to be resolved from the background in the near-future (see Figure 11).
- **Other GW detectors** include Doppler ranging to spacecraft in the solar system (Armstrong 2006), however projections based on populations and future spacecraft missions to the Ice-Giant planets suggest that a factor of ~ 100 improvement in sensitivity is required for these experiments to detect SMBHB mergers and contribute to, e.g., source localization (Soyuer et al. 2021). Relative astrometric tracking of a large field of stars is also promising for detecting low-frequency GWs via the quadrupolar motions imprinted on the stellar positions. Upon its final data release, *Gaia* may yield constraints of a GW background via high precision astrometric tracking of stars in the Galaxy, covering frequencies at the high end of the PTA band and higher (Moore et al. 2017). Additionally, the Roman Space Telescope may be able to probe the frequency gap between LISA and PTAs and measure the high frequency end of a gravitational wave background from SMBHBs (Pardo et al. 2023).

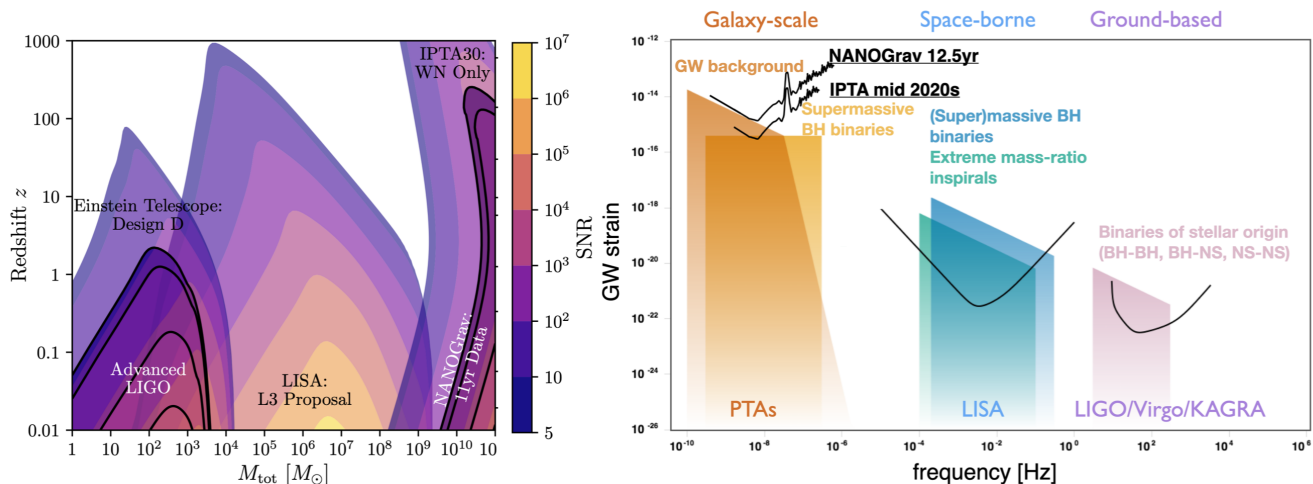


Figure 11. *Left:* Signal-to-noise ratio of binaries across GW detectors as a function of total mass and redshift, adapted from Kaiser & McWilliams (2021) *Right:* Overview of the GW spectrum, detectors and source populations as a function of GW frequency, adapted from Moore et al. (2015).

Space-borne Interferometers and LISA

In order to extend interferometric GW detectors, like the ground-based LIGO, to the lower frequencies needed to detect mergers of $10^4 - 10^7 M_{\odot}$ SMBHBs, longer interferometer arm lengths are required, along with reduced Earth-related noise sources prevalent at these frequencies (Amaro-Seoane et al. 2017). Hence, planned \sim mHz frequency GW observatories will be space-borne. Here we focus on the joint ESA+NASA mission, LISA. LISA is nominally a four year mission that will consist of three spacecrafts in Earth-trailing orbits comprising a constellation composing the vertices of an equilateral triangle with 2.5×10^6 km length arms (Amaro-Seoane et al. 2017). From 2015-2017, the LISA Pathfinder tested key technologies for the mission, outperforming required specifications (e.g., Armano et al. 2018), and leading the way for the full LISA mission, scheduled to launch in the early-mid 2030s.

LISA will be sensitive to a variety of GW sources including BH mergers with total masses ranging from $100 M_{\odot}$ up to $10^7 M_{\odot}$. An overview of these sources and LISA science topics is provided in Amaro-Seoane et al. (2023). Here we briefly review the expected LISA merger rates for the SMBHBs relevant to this Chapter.

LISA merger rates are estimated by implementing choices for the seeding of SMBHBs in galaxies and then following the subsequent evolution of the SMBHB pairs, *i.e.*, modeling the processes described in §2. This is done through a combination of semi-analytical treatments (e.g., Ricarte & Natarajan 2018; Dayal et al. 2019; Barausse et al. 2020) and sub-grid prescriptions paired with full hydrodynamical cosmological simulations (e.g., Salcido et al. 2016; Tremmel et al. 2018; Volonteri et al. 2020; Katz et al. 2020) – a detailed overview is given in §2.4 of Amaro-Seoane et al. (2023). These studies predict merger rates ranging from ~ 1 up to a few hundred per year out to maximum redshifts ranging from $z \sim 1$ to $z \sim 20$.

The uncertainties in these estimates are highly dependent on seed masses of the SMBHBs at birth, as well as on choices for SMBH growth through accretion over time, the effects of feedback onto the surrounding environment, the dynamics of the binary evolution and inspiral (e.g., Bonetti et al. 2019), as well as a number of other more subtle choices that could affect, e.g., the retention of SMBHBs after merger due to GW recoil (e.g., Izquierdo-Villalba et al. 2020).

While sensitive dependence on physical parameters in models means that large uncertainties arise in predicted merger rates (and merger demographics), it also means that a measurement of the merger rate by LISA could constrain some aspects of these models. In addition to measuring merger rates, LISA will follow SMBHB inspirals for days to months before merger, observing possibly up to $\sim 10^5$ cycles (Amaro-Seoane et al. 2017). Long durations in band (compared to, e.g., sub-second, ~ 10 's of cycles detections with the current ground based detectors), coupled with the LISA sensitivity, results in high signal-to-noise ratio detections for SMBHBs (Figure 11). This means that LISA will be capable of measuring the orbital parameters of individual systems to high precision and so provide the possibility of providing distributions of merging binary parameters that may be compared with predictions from formation and evolution models. This is analogous to the current efforts to understand the observed stellar-mass binary-BH mergers (The LIGO Scientific Collaboration et al. 2021) from individual and population

masses, spins, or eccentricities. LISA could make more precise system measurements (given the much higher predicted signal-to-noise ratios), compared to current capabilities of ground-based detectors, though likely for fewer systems (given the expected rates).

Pulsar Timing Arrays (PTAs)

A PTA is a galactic scale GW detector that relies on precise measurements of milli-second pulsars (Taylor 2021). These magnetized neutron stars have collimated emission along the magnetic axis, and are very stable rotators. If the rotation axis is misaligned with the radiation axis, the radiation can periodically sweep our our line-of-sight, allowing us to observe a series of precisely repeating radio pulses. If GWs from SMBHBs pass through the Galaxy, they perturb the Earth-pulsar distance, and induce coherent deviations in the arrival time of these radio signals. The GWs affect many pulsars and deviations should be detectable in many pulsars in the array. They should also be spatially correlated with a characteristic quadrupolar pattern, known as the Hellings & Downs curve (Hellings & Downs 1983).

Currently, three main collaborations, the North American Nanohertz Observatory for Gravitational waves (NANOGrav; McLaughlin 2013), the European Pulsar Timing Array (EPTA; Kramer & Champion 2013) and the Parkes Pulsar Timing Array (PPTA; Hobbs 2013), are systematically monitoring milli-second pulsars with the aim to detect low-frequency GWs. These, along with newer PTA collaborations, like the Indian Pulsar Timing Array (InPTA; Joshi et al. 2018), the Chinese Pulsar Timing Array (CPTA; Lee 2016) and the MeerKAT Pulsar Timing Array (Bailes et al. 2020) work together under the auspices of an international consortium, the International Pulsar Timing Array (IPTA; Hobbs et al. 2010).

All major PTA collaborations have recently reported evidence for a stochastic GW background with a significance between 3 and 4 σ for the characteristic Hellings & Downs interpulsar correlations (Agazie et al. 2023c; EPTA Collaboration et al. 2023; Reardon et al. 2023; Xu et al. 2023). The results are broadly consistent between the different PTAs, despite differences in the datasets and data analysis methods (The International Pulsar Timing Array Collaboration et al. 2023). Even though the origin of the signal is still uncertain, the background (or at least a fraction of it) is likely produced by SMBHBs throughout the universe, and can be successfully modeled with an astrophysically motivated population of SMBHBs (Agazie et al. 2023b; Antoniadis et al. 2023b). The amplitude of the GW background can constrain the merger rate of massive galaxies, the SMBH mass function, and the rate of binary formation in post-merger galaxies. The shape of the GW spectrum depends on the highly uncertain orbital evolution of SMBHBs, along with orbital properties of the population of binaries, *e.g.*, circular versus eccentric binary orbits (Taylor et al. 2019; Burke-Spolaor et al. 2019).

The relatively high recovered amplitude (at the high end of theoretical expectations, *e.g.*, see Fig. A1 in Agazie et al. 2023b) suggests efficient mergers occurring in high-mass systems. In particular, sampling the binary population parameter space with Markov Chain Monte Carlo methods to fit the GW background spectrum favors galaxy and SMBH mass functions that are towards the higher end of previous expectations (although these two parameters are degenerate) and disfavors long binary lifetimes spanning from the large separations to the PTA band. Moreover, the background spectrum shows a turnover at the lowest frequencies indicative of binary evolution driven by environmental interactions. We note, however, that we are still in the low-signal-to-noise ratio (S/N) regime regarding the GW background and thus the population inference is sensitive to choices of the GW data analysis. Therefore, some of the above conclusions may change in the future, as the S/N increases and we are able to better characterize the background. We emphasize that, despite significant uncertainties, the GW background is the best observational evidence so far that SMBHBs form and evolve into the GW regime and eventually coalesce.

Theoretical models predict that signals from individually resolved sources can be detected on top of this background in just a few years (Rosado et al. 2015; Mingarelli et al. 2017; Kelley et al. 2018; Taylor et al. 2020). Individually resolved signals produced by massive and relatively nearby binaries will open up the possibility for multi-messenger observations combining electromagnetic and GW data (*e.g.*, Kelley et al. 2019a; Charisi et al. 2022, but see also §4.3). Since PTAs detect the early stages of GW inspiral thousands of years before coalescence, these binaries evolve slowly resulting in nearly monochromatic GW signals (over the observed baseline of observations), with long-lived electromagnetic counterparts, likely the SMBHB signatures described above. Therefore, the detection of individually resolved SMBHBs and the subsequent multi-messenger observations will allow us to probe in detail models of binary emission. Note that the slow evolution of binaries over thousands of years may be detectable via the pulsar terms, which trace the GW signal at the location of the pulsars (at kpc distances) (*e.g.*, Corbin & Cornish 2010; McGrath & Creighton 2021). Already PTA limits on individually resolved binaries have provided important astrophysical constraints (Arzoumanian et al. 2023; Falxa et al. 2023; Agazie et al. 2023a; Antoniadis et al. 2023a) including stringent mass ratio upper limits on galaxies in the nearby universe (Arzoumanian et al. 2021), which for some galaxies are comparable to the limits we can place on a binary companion to Sgr A* (Will et al. 2023).

PTAs have recently opened a new window to the GW spectrum finding evidence for a stochastic GW background likely produced by a population of SMBHBs. The detection of individually resolved binaries should follow soon after. Finally, PTAs in the future could explore the spatial anisotropy of the GW background (Ravi et al. 2012; Mingarelli et al. 2013; Sato-Polito & Kamionkowski 2023; Gardiner et al. 2023; Agazie et al. 2023d), measure cosmological parameters (D’Orazio & Loeb 2021; McGrath et al. 2022; Wang et al. 2022a), probe alternative theories of gravity, and constrain the density of cosmic strings and more (Burke-Spolaor et al. 2019).

Pros and Cons: Gravitational Waves

Pros:

- GW detection is a direct method.
- PTAs have recently detected evidence for the stochastic GW background, consistent with production by low-frequency GWs from inspiralling SMBHBs.
- GW detections with PTAs and LISA will provide definitive measurements of SMBHB merger rates, which will anchor the binary formation and evolution models.

Cons:

- The rates for individually resolved binaries in PTAs and LISA are highly uncertain.
- Even in the most optimistic scenarios, PTAs are expected to detect only a handful of binaries in the relatively near future.
- LISA is at least 10 years away.
- GWs access only the end states of the SMBHB evolution, though this reaches up to $\sim 0.01 - 0.1$ pc separations for the most massive SMBHBs constrained by PTAs.

4. FUTURE PROSPECTS

We now highlight and expand upon a few future directions that we find particularly interesting.

4.1. Electromagnetic Time-domain Surveys

LSST with its unprecedented quantity and quality of data will revolutionize the search for SMBHBs. It will deliver a massive sample of millions of quasars, enabling the detection of rare binaries, while the exceptional sampling of the lightcurves will lead to minimal false detections (see Figure 12).

The upcoming LSST will offer a major improvement in the observations of quasars in both survey area and depth. Early estimates of the LSST quasar population ranged from 8.4 million, for the limiting magnitude of $m = 24$, achieved in a single-night LSST visit with two exposures, to 16.7 million at the full survey depth of $m = 26$ achieved with co-addition of multiple epochs (Ivezić et al. 2019). Revised estimates based on a recently updated luminosity function (Kulkarni et al. 2019) predict about six times more quasars ranging from 19-100 million quasars at $m = 24$ and $m = 26$, respectively (Xin & Haiman 2021). The single-night limit is important for the purposes of periodicity detection, since the higher depth is achieved through co-adding of multiple images and does not allow for variability studies.

LSST will provide a large sample of quasars, in which exceedingly rare short-period binaries with periods of a few days to a few weeks will be abundant. In fact, such short-period binaries will be the sweet spot for discovery in LSST, since many cycles will repeat within the data, even with the baselines from the first few data releases. For instance,

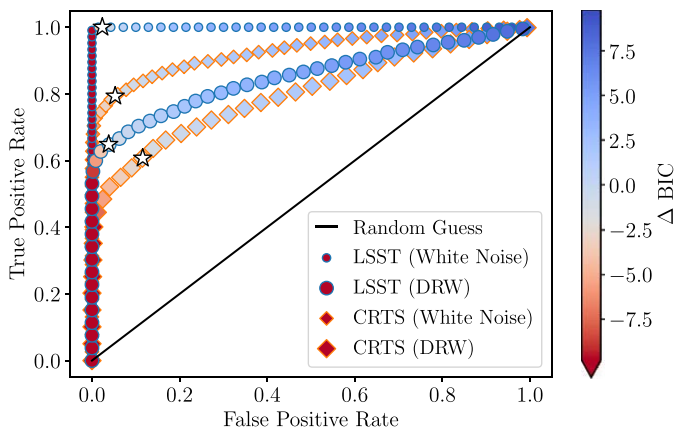


Figure 12. True positive vs. False positive rate for detection of periodic signatures in noisy data, considering both white and DRW noise. There is an obvious improvement with LSST vs. CRTS (Djorgovski et al. 2011). From Witt et al. (2022).

For instance,

Xin & Haiman (2021) estimated that 30-150 ultra-short period binaries (with observed period $P < 1$ day) should be detectable in LSST. Since binaries spend more time at wider separations (and longer orbital periods), they predicted the detection of order $10^3 - 10^4$ binaries with periods 30-100 days considering the nightly flux limit ($m = 24$). Additional theoretical models predict that a few hundred binaries should be detectable through the self-lensing signature (D’Orazio & Di Stefano 2018) or due to relativistic Doppler boost (Kelley et al. 2019b, 2021).

Another major advantage of LSST will be its dense temporal coverage. Most of the survey time will be spent on the deep-wide-fast survey mode, which will cover the 18,000 deg² footprint with a semi-regular cadence, with repeat observations every three to five nights. This strategy will return high-quality lightcurves with dense sampling, ideal for periodicity detection. In addition, observations will alternate among six narrow-band optical filters providing invaluable color information (though making the cadence in a single color lower than once per three-five nights). Witt et al. (2022) demonstrated that the quality of the LSST lightcurves is truly a game changer in periodicity searches returning a minimal contamination with false detections; the false positive rate is significantly reduced compared to CRTS (see Figure 12).

The High Latitude Time Domain Survey of the planned Roman Space Telescope will cover a smaller area of the sky (~ 19 deg²) but will go much deeper than LSST, reaching $m = 28$ in a single epoch, or $m = 30$ co-added. Haiman et al. (2023) predict that a four month survey would detect ~ 100 periodic quasars. Requiring observations of 10 cycles, this allows maximum periods of ~ 12 days, while rarity of shorter period SMBHBs and survey cadence limit to ~ 5 days for the shortest detectable periods. The depth of a Roman survey would uniquely allow discovery of systems powered by SMBHBs in the $10^{4-6} M_{\odot}$ range, which will merge in the LISA band after 10^{3-5} yrs (Haiman et al. 2023).

We also note that an X-ray Survey mission (the proposed Star-X mission, e.g., Zhang et al. 2022) would benefit periodicity searches, especially for self-lensing signatures where emission coming from a small region near the SMBH can be the most magnified.

4.2. Direct Orbital Tracking with High-angular Resolution Experiments

As discussed in §3.6, present and next-generation VLBI experiments and the GRAVITY+ optical interferometer will be able to access μas scales subtended by sub-parsec separation SMBHBs, via imaging and astrometric photo-center tracking. While difficult, the astrometric or resolved tracking of an SMBHB orbit over the course of a period offers what many other methods do not, an unambiguous electromagnetic identification of a sub-parsec separation SMBHB. This definitive detection could help us to build a detection ladder by studying the properties of the system on all scales and wavelengths and to possibly use this information to devise new search methods. With enough definitively identified SMBHB systems, we may be able to start characterizing how SMBHB-harboring galaxies differ in their properties, if at all, from the “normal quasars.”

4.3. Low-frequency Gravitational Wave Experiments & Multi-messenger Promise

As mentioned above, PTAs have already reached a milestone by finding evidence for the low-frequency GW background in the nanohertz band, the significance of which is expected to grow in the upcoming years leading to a definitive detection. Upper limits on the GW background had already provided significant constraints onto the population of binary candidates detected in time-domain surveys (Sesana et al. 2018; Holgado et al. 2018). These multi-messenger consistency checks on close-separation SMBHB candidates will become even more powerful in vetting the candidate population, as the PTA sensitivity increases and the background is measured across the PTA frequency range. Several factors contribute to the expected PTA sensitivity increase, such as: (1) the pulsars are monitored for longer baselines enabling us to probe lower frequencies of the GW spectrum, (2) technological advances in the radio receivers reduce the noise of observations, (3) more advanced statistical techniques are employed for the analysis of the data, (4) more and higher quality pulsars are discovered and are systematically monitored. The combination of multiple datasets, e.g., from individual PTAs into a common International PTA dataset can also boost the sensitivity. In addition, existing radio telescopes like the Canadian Hydrogen Intensity Mapping Experiment (CHIME; CHIME/Pulsar Collaboration et al. 2021) and the Five-hundred-meter Aperture Spherical Telescope (FAST; Hobbs et al. 2019), along with future radio observatories, like ngVLA (Burke-Spolaor et al. 2018), the Deep Synoptic Array (DSA-2000; Hallinan et al. 2019), and the Square Kilometer Array (SKA; Stappers et al. 2018) are expected to vastly increase the number of detected and monitored pulsars, greatly improving the sensitivity of PTAs.

Given the discovery of evidence for the GW background, PTAs are also expected to detect GWs from individual SMBHBs that produce signals strong enough to stand above the background (Rosado et al. 2015; Mingarelli et al. 2017; Kelley et al. 2018; Taylor et al. 2020). Since SMBHBs are expected to emit both bright electromagnetic signals and strong GWs, they make exceptional targets for multi-messenger observations (Sesana et al. 2012; Kelley et al. 2019a; Baker et al. 2019; Charisi et al. 2022). Multi-messenger observations will offer significant advantages in constraining the dynamical interaction of binaries

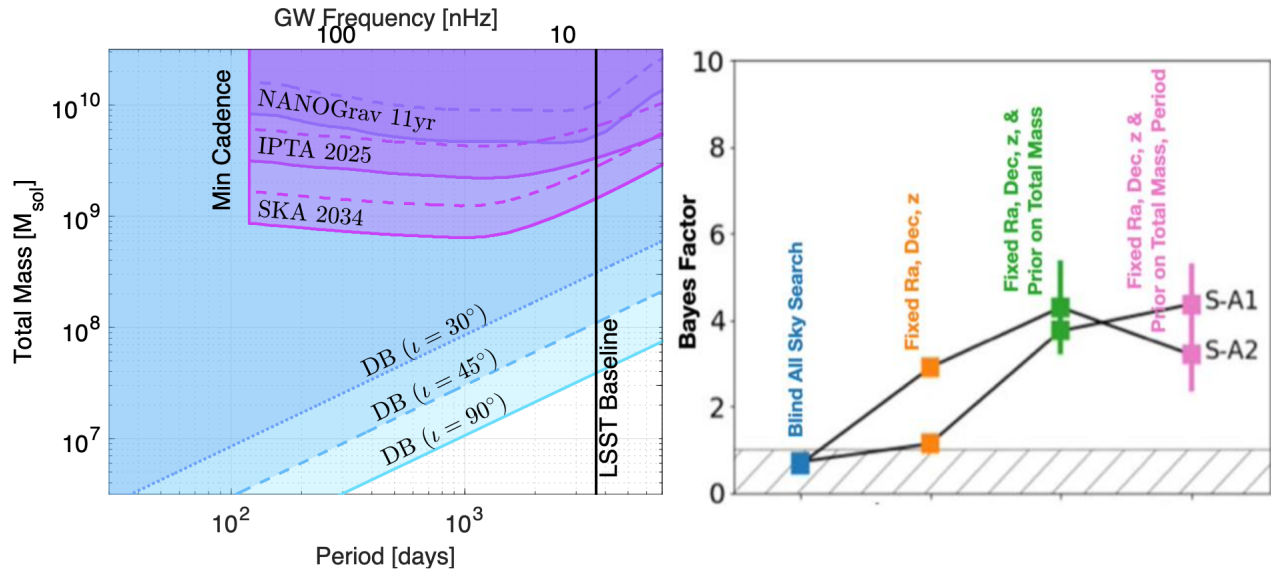


Figure 13. *Left:* Binary parameter space for which multi-messenger observations with time-domain surveys and PTAs are possible. The blue shaded regions show EM detectable binaries with peak-to-peak Doppler boost variability $\geq 10\%$ for different inclinations and fixed mass ratio of $q = 1/4$. The purple shaded regions delineate the GW detectability of binaries of the same mass ratio with current and projected PTA sensitivity. From Charisi et al. (2022) *Right:* Comparison of Bayes factors for GW detection between completely uninformed all-sky searches and searches with some prior information about the host galaxy or the binary. Adapted from Liu & Vigeland (2021).

with their environment, unveiling the physics of accretion in the presence of binaries, and probing the co-evolution of SMBHBs with their host galaxies, and more (Kelley et al. 2019a). PTAs and current electromagnetic time-domain surveys probe the overlapping populations of SMBHBs, i.e. binaries with similar periods and masses (see Figure 1, and Charisi et al. 2022). In Figure 13, we show the parameter space of SMBHBs, where multi-messenger observations are possible given current and future PTA capabilities. Combining electromagnetic and PTA data has great advantages; incorporating binary orbital constraints from electromagnetic observations (e.g., period/mass of a candidate) can improve GW upper limits by a factor of two (Arzoumanian et al. 2020).

Similarly, including priors from electromagnetic data in PTA searches can boost the detectability of binaries and improve parameter estimation (Liu & Vigeland 2021; Liu et al. 2023; Charisi et al. 2023). In the right panel of Figure 13, we show the Bayes factor for GW detection for simulated binaries injected in a PTA that resembles the NANOGrav 11yr dataset. The detectability of the same binary increases when prior information e.g., known from an electromagnetic candidate is included in the search. In the case of the Doppler boost (and self-lensing) variability, the PTA signal can be directly linked to the periodicity of a quasar candidate for a multi-messenger data stream (Charisi et al. 2022), potentially allowing for further boost in the detectability of the source and its parameter estimation.

In the LISA-era of the next decade, electromagnetic counterparts due to a plethora of sources have been and continue to be explored, including circumbinary disk and mini-disk interactions, Doppler boosting and jet launching in the moments before and through merger (Palenzuela et al. 2010; Noble et al. 2012; Moesta et al. 2012; Gold et al. 2014a,b; Tang et al. 2018; Farris et al. 2015a; Kelly et al. 2017; Haiman 2017; Khan et al. 2018; d’Ascoli et al. 2018; Kelly et al. 2021; Gutiérrez et al. 2022; Bright & Paschalidis 2023; Wang et al. 2023c) as well as post-merger GW recoil induced shocks (Lippai et al. 2008; Corrales et al. 2010; Rossi et al. 2010; Meliani et al. 2017; Krauth et al. 2023). If one of these electromagnetic signatures arises, we can only observe it if we know in advance which direction on the sky to point telescopes. Mangiagli et al. (2020) considers LISA’s ability to localize a GW source on the sky in time to follow up with electromagnetic observations and follow up work (Mangiagli et al. 2022) considers optical, radio, and X-ray counterparts to SMBHB mergers and determines detectability with joint LSST plus LISA, the Square Kilometer Array (SKA Dewdney et al. 2009) plus the European Extremely Large Telescope (E-ELT 2023) plus LISA, or Athena (Nandra et al. 2013) plus E-ELT plus LISA configurations. They determine that a few such electromagnetic counterparts to SMBHB mergers may be detectable during a four year LISA mission. Further possibilities with X-ray and GW joint detections with a LISA and Athena are detailed in Piro et al. (2023).

5. SUMMARY OF OBSERVATIONAL SEARCHES AND CANDIDATES

Below we summarize the observational efforts to uncover SMBHB candidates based on the signatures described in this Chapter.

5.1. Searches and candidates from spectroscopic signatures

5.1.1. Systematic Searches for Broad Emission Line Shifts in Optical Spectra from SDSS

- [Tsalmantza et al. \(2011\)](#): Search for broad lines offset with respect to narrow lines in $\sim 59,000$ quasars with $0.1 < z < 1.5$ revealed 34 sources with peculiar spectra, of which 9 are binary candidates (4 new, and 5 previously known).
- [Eracleous et al. \(2012\)](#): Search for displaced broad $H\beta$ lines in 15,900 quasars with $z < 0.7$ found 88 candidates (some previously known). Of those, 68 candidates were followed-up revealing significant velocity shifts in 14.
- [Ju et al. \(2013\)](#): Search for velocity shifts in broad Mg II lines in > 1500 quasars with $0.36 < z < 2$ and multiple spectra detected 7 (64) strong (possible) candidates. They inferred that $\leq 18\%$ of quasars can host binaries.
- [Shen et al. \(2013\)](#): Search for broad $H\beta$ line shifts in 700 quasars with $z < 0.7$ and multiple spectra revealed 28 sources, of which 7 are top binary candidates. If variability is due to binaries and not intrinsic, most quasars should harbor SMBHBs.
- [Liu et al. \(2014b\)](#): Search for displaced $H\beta$ broad lines in $\sim 21,000$ quasars found 399 candidates, of which 50 were followed-up revealing 24 sources with significant radial accelerations and 9 were considered top binary candidates. Unlike previous studies *e.g.*, [Eracleous et al. \(2012\)](#), moderate velocity offsets ($< 1000\text{km/s}$) were also considered.

5.1.2. Spectroscopic Follow-up of Candidates Identified in Systematic Searches

- [Decarli et al. \(2013\)](#): Follow-up of the [Tsalmantza et al. \(2011\)](#) sample found significant line variations in 11 sources. It is unclear whether the variability is coherent as expected for binaries or transient and longer monitoring is required.
- [Runnoe et al. \(2015, 2017\)](#): Follow-up of the [Eracleous et al. \(2012\)](#) sample over 12 years with 3-4 observations per source. Radial velocity curves can be constructed for 29 sources with 3 candidates showing monotonic velocity changes. Limits on binary parameters cannot exclude any of the candidates, but this will change with longer baselines.
- [Wang et al. \(2017\)](#): Follow-up of 21 candidates of the [Ju et al. \(2013\)](#) sample found that none is consistent with the binary scenario. The search was repeated in a sample ~ 1400 quasars with multi-epoch spectra spanning 10 years from BOSS and revealed one candidate. They concluded that $\leq 1\%$ of the quasars host binaries with separation of order ~ 0.1 pc.
- [Guo et al. \(2019\)](#): Follow-up of 52 candidates in [Shen et al. \(2013\)](#); [Liu et al. \(2014b\)](#) showed that 5 sources are viable candidates based on their radial velocity curves, concluding that $\sim 13\%$ of quasars are associated with sub-parsec binaries.

5.1.3. Individual Candidates Primarily from Early SDSS Studies

- J0927+2943: Highly blue-shifted Balmer lines could indicate a recoiling SMBH ([Komossa et al. 2008](#)) or an SMBHB ([Dotti et al. 2009](#); [Bogdanović et al. 2009](#)), but both hypotheses were later disfavored by [Decarli et al. \(2014\)](#).
- J1536+0441: Candidate identified by atypical spectrum with two broad emission line systems ([Boroson & Lauer 2009](#)).
- J1050+3456: Candidate with blue-shifted Balmer lines, but could be a double-peaked emitter ([Shields et al. 2009](#)).
- J1000+2233: A binary was invoked to explain extreme velocity offsets in $H\alpha$ and $H\beta$ lines ([Decarli et al. 2010](#)).
- J0932+0318: Similar to J1050+3456, double-peaked emission is a possible alternative to binarity ([Barrows et al. 2011](#)).
- NGC4151: Lightcurve and radial velocity curve could be explained by an eccentric binary candidate ([Bon et al. 2012](#)).
- Mrk 231: The observed flux deficit in the UV/optical spectrum was associated with a cavity in a circumbinary disk ([Yan et al. 2015](#)), but dust reddening can better explain the entire spectrum ([Leighly et al. 2016](#)).

5.1.4. Candidates with Double-peaked Spectra and Follow-ups

- Quasars with double-peaked broad emission lines, like QSO OX 169, Arp 102B, 3C 390.3, 3C 332 were proposed as binary candidates ([Gaskell 1983](#); [Stockton & Farnham 1991](#); [Gaskell 1996](#)).
- Subsequent follow-up monitoring of the above and many other similar sources disfavored the SMBHB interpretation for this class of quasars, known as double-peaked emitters. The line variability is inconsistent with expectations for binaries and they can be more naturally explained by disks around single-SMBHBs ([Halpern & Filippenko 1988](#); [Eracleous & Halpern 1994](#); [Eracleous et al. 1997](#); [Eracleous & Halpern 2003](#); [Eracleous et al. 2009](#); [Liu et al. 2016](#); [Doan et al. 2020](#)).

5.2. Searches and Candidates from Photometric Signatures

5.2.1. Systematic Searches in Time-domain Surveys

- [Graham et al. \(2015b\)](#): Search in a sample of 243,500 spectroscopically confirmed in CRTS revealed 111 candidates with periods of 650-2500 d. The lightcurves of the candidates were extended with data from LINEAR when available.
- [Charisi et al. \(2016\)](#): Search in a sample of 35,383 quasars in PTF selected 50 candidates with periods of 130-900 d, 33 of which remain statistically significant after the re-analysis of extended lightcurves with data from CRTS and iPTF.
- [Liu et al. \(2019\)](#): Search in a sample of 9000 quasars from Pan-STARRS MDS selected 26 candidates with periods of 300-1000 d, but follow-up monitoring with the Discovery Channel Telescope and LCO excluded all but one candidate.
- [Chen et al. \(2020\)](#): Search in a sample of 625 quasars in overlapping DES+SDSS stripe 82 fields with long baseline lightcurves (20yr) detected 5 candidates with periods of 3-5 yr.
- [Chen et al. \(2022b\)](#): Search in 143,700 quasars from ZTF detected 127 candidates with periods of 500-1000 d.
- [Serafinelli et al. \(2020\)](#); [Liu et al. \(2020\)](#) Two independent searches in Swift/BAT 105-month survey. The former analyzed 553 quasars, found a new candidate, and validated a known one (MCG+11-11-032). The latter analyzed 941 quasars and found no evidence for periodicity including the previously known candidate.
- [Sandrinelli et al. \(2018\)](#); [Holgado et al. \(2018\)](#): These two studies (and references therein) summarize the binary candidates identified from their quasi-periodic behaviour in Fermi gamma-ray lightcurves.

5.2.2. Periodic Candidates Identified Individually

- Optical:
 - OJ 287: This bright blazar has a lightcurve spanning a century (albeit sparse initially) with quasi-periodicity of 11.86yr and twin flares 1yr apart. The periodicity is explained by an eccentric and unequal mass binary; the flares are produced every time the secondary plunges through the primary's accretion disk on a relativistically precessing orbit ([Valtonen et al. 2008](#); [Komossa et al. 2021](#)). The most recently expected flare, however, was not confirmed by observations ([Komossa et al. 2023a](#); [Valtonen et al. 2023](#)).
 - PG 1302-102: The first candidate found in the recent systematic searches ([Graham et al. 2015b](#)). Because of its brightness it allowed for extensive follow-up studies, which potentially reveal additional evidence for its binary nature.
 - SDSS J0159+0105: This candidate was detected in CRTS, although it was not selected by [Graham et al. \(2015b\)](#). It has two periods (741 and 1500 days) and was interpreted as having the predicted by simulations 2:1 period ratio. The broad H β line exhibits variability and it has unusually bright UV spectrum ([Zheng et al. 2016](#)).
 - Q J0158-4325: Periodicity of ~ 176 d was detected in this microlensed quasar ([Millon et al. 2022](#)).
 - J025214.67-002813.7: One of the 5 candidates detected in DES+SDSS search with a period of 1607 d was associated with accretion variability models ([Liao et al. 2021](#)).
 - Spikey: This candidate was identified from its symmetric flare ([Hu et al. 2020](#)). The variability is well fit by an eccentric self-lensing model, but its periodicity has not been confirmed yet.
- Radio:
 - PKS 2131-021: This candidate has a periodicity of 1729 d in the 14.5-15.5 GHz lightcurves, and was first put forth by [Ren et al. \(2021\)](#). The periodicity disappears and appears almost in phase at a later epoch and was interpreted with a jet-Doppler model by [O'Neill et al. \(2022\)](#).
- Gamma Rays:
 - PG 1553+113: The first gamma-ray variable blazar with a detected periodicity of 2.18 y in rest frame ($z = 1.285$) ([Ackermann et al. 2015](#); [Sandrinelli et al. 2018](#)) has prompted many multi-wavelength follow-up studies.
 - PKS 2247-131: A 34.5 period was attributed to jet helicity due to an orbiting SMBHB ([Zhou et al. 2018](#)).
 - PKS 2155-304: A periodicity of 620 d was detected in this candidate ([Sandrinelli et al. 2018](#)).
 - BL Lac: Candidate identified from periodicity of 1.86 yr [Sandrinelli et al. \(2018\)](#).

5.3. Candidates from Jet Signatures

5.3.1. Individual Candidates with Helical or Periodic Jet Structures

- S5 1928+738: The helical structure and periodic components of the jet can be explained by the orbital motion of the jet-launching SMBH in a binary system (Roos et al. 1993; Kun et al. 2014).
- Mkn 501: A binary model could explain the complex structure of the curved helical jet (Villata & Raiteri 1999).
- 3C 273: The rapid jet precession may be due to precession of in the inner accretion disk induced by a second SMBH in a non-co-planar orbit (Abraham & Romero 1999; Romero et al. 2000).
- PKS 0420-014: A binary model can explain the motion of jet components on helical trajectories (Britzen et al. 2001).
- BL Lacertae (2200+420): A straight jet precessing with a short period could be caused by an SMBHB (Stirling et al. 2003), in which the jet is associated with the secondary (less massive) SMBH (Caproni et al. 2013).
- 3C 120: A binary was invoked to explain the helical jet structure and optical periodicity (Caproni & Abraham 2004a).
- AGN 1156+295: The oscillatory pattern in the jet could be explained by a binary candidate (Hong et al. 2004), but follow-up observations are more consistent with a Kelvin Helmholtz instability (Zhao et al. 2011).
- 3C 345: The position and velocity of multiple jet components suggest a wobbling jet with a short precession period consistent with an SMBHB (Caproni & Abraham 2004b; Lobanov & Roland 2005; Qian et al. 2009).
- PKS 1830-211: The helical jet may be caused by rapid precession due to an SMBHB (Nair et al. 2005).
- S5 1803+784: A binary was proposed to explain the evolution of the VLBI coordinates of a single jet component (Roland et al. 2008), but none of the existing models can explain all the jet properties (Britzen et al. 2010).
- B1308+326: The kinematics of multiple jet components can be explained by jet precession due to an SMBHB, but other explanations (*e.g.*, spin precession of a single SMBH) are also possible (Qian et al. 2017).
- 3C 279: The complex jet structure of this candidate is consistent with two precessing jets with the same period but different orientations (Qian et al. 2019), but detailed observations by EHT challenge this model (Kim et al. 2020).
- 3C 454.3: The kinematic behavior of multiple jet components suggests the existence of two groups of knots produced by a double-jet in a binary system (Qian et al. 2021).
- 4C31.61 (2201+315): The jet structure can be explained by a system of three distinct jets, associated with three SMBHs separated by $\sim 1 - 2$ pc (Roland et al. 2020).
- Britzen et al. (2023) apply jet precession models to OJ 287 as well as 11 other quasars listed in their Table 6 (3C 279, 3C 273, PKS 0735+178, 2200+420, PG 1553+113, 3C 345, 3C 120, 1308+326, TXS 0506+056, 3C 84, PKS 1502+106).

5.3.2. Follow-up of Candidates Selected with Other Methods

- Spikey: VLBI images show a wiggly jet structure consistent with the binary scenario (Kun et al. 2020).
- PG1302: The morphology of the jet at kilo-parsec scale along with parsec scale kinematics support the binary scenario for this candidate (Kun et al. 2015; Mohan et al. 2016).
- OJ287: The highly variable jet of this source can be fit by a helical model produced by the binary orbital motion Valtonen & Pihajoki (2013).
- PG1553: The kinematics of several jet components suggest a precessing jet consistent with the periodicity detected in the gamma-ray lightcurve (Caproni et al. 2017).

5.3.3. X and Z-shaped Jets

- Yang et al. (2019) present a catalog of 290 “winged” or X-shaped radio galaxies.

ACKNOWLEDGMENTS

The authors would like to thank Jessie Runnoe, Aaron Stemo for comments on an early version of the manuscript. D.J.D. received funding from the European Union’s Horizon 2020 research and innovation programme under Marie Skłodowska-Curie grant agreement No. 101029157, and from the Danish Independent Research Fund through Sapere Aude Starting Grant No. 121587. MC acknowledges support from NSF award AST-2007993.

REFERENCES

- Abraham, Z., & Romero, G. E. 1999, *A&A*, 344, 61
- Ackermann, M., Ajello, M., Albert, A., et al. 2015, *ApJL*, 813, L41
- Agazie, G., Anumarlapudi, A., Archibald, A. M., et al. 2023a, *ApJL*, 951, L50
- . 2023b, *ApJL*, 952, L37
- . 2023c, *ApJL*, 951, L8
- . 2023d, *ApJL*, 956, L3
- Amaro-Seoane, P., Audley, H., Babak, S., et al. 2017, arXiv e-prints, arXiv:1702.00786
- Amaro-Seoane, P., Andrews, J., Arca Sedda, M., et al. 2023, *Living Reviews in Relativity*, 26, 2
- Antoniadis, J., Arumugam, P., Arumugam, S., et al. 2023a, arXiv e-prints, arXiv:2306.16226
- . 2023b, arXiv e-prints, arXiv:2306.16227
- Arcavi, I., Gal-Yam, A., Sullivan, M., et al. 2014, *ApJ*, 793, 38
- Armano, M., Audley, H., Baird, J., et al. 2018, *PhRvL*, 120, 061101
- Armstrong, J. W. 2006, *Living Reviews in Relativity*, 9, 1
- Arzoumanian, Z., Baker, P. T., Brazier, A., et al. 2020, *ApJ*, 900, 102
- . 2021, *ApJ*, 914, 121
- Arzoumanian, Z., Baker, P. T., Blecha, L., et al. 2023, *ApJL*, 951, L28
- Atwood, W. B., Abdo, A. A., Ackermann, M., et al. 2009, *ApJ*, 697, 1071
- Azadi, M., Coil, A. L., Aird, J., et al. 2017, *ApJ*, 835, 27
- Bailes, M., Jameson, A., Abbate, F., et al. 2020, *PASA*, 37, e028
- Baker, J., Haiman, Z., Rossi, E. M., et al. 2019, *BAAS*, 51, 123
- Bansal, K., Taylor, G. B., Peck, A. B., Zavala, R. T., & Romani, R. W. 2017, *ApJ*, 843, 14
- Barausse, E., Dvorkin, I., Tremmel, M., Volonteri, M., & Bonetti, M. 2020, *ApJ*, 904, 16
- Barnes, J. E. 2002, *MNRAS*, 333, 481
- Barnes, J. E., & Hernquist, L. 1996, *ApJ*, 471, 115
- Barrows, R. S., Lacy, C. H. S., Kennefick, D., Kennefick, J., & Seigar, M. S. 2011, *NewA*, 16, 122
- Begelman, M. C., Blandford, R. D., & Rees, M. J. 1980, *Nature*, 287, 307
- Blundell, K. M., Laing, R., Lee, S., & Richards, A. 2018, *ApJL*, 867, L25
- Bogdanović, T., Eracleous, M., & Sigurdsson, S. 2009, *ApJ*, 697, 288
- Bogdanović, T., Miller, M. C., & Blecha, L. 2022, *Living Reviews in Relativity*, 25, 3
- Bogdanović, T., Smith, B. D., Sigurdsson, S., & Eracleous, M. 2008, *ApJS*, 174, 455
- Bon, E., Jovanović, P., Marziani, P., et al. 2012, *ApJ*, 759, 118
- Bonetti, M., Sesana, A., Haardt, F., Barausse, E., & Colpi, M. 2019, *MNRAS*, 486, 4044
- Boroson, T. A., & Lauer, T. R. 2009, *Nature*, 458, 53
- Bortolas, E., Franchini, A., Bonetti, M., & Sesana, A. 2021, *ApJL*, 918, L15
- Bortolas, E., Mapelli, M., & Spera, M. 2018, *MNRAS*, 474, 1054
- Bright, J. C., & Paschalidis, V. 2023, *MNRAS*, 520, 392
- Britzen, S., Roland, J., Laskar, J., et al. 2001, *A&A*, 374, 784
- Britzen, S., Zajaček, M., Gopal-Krishna, et al. 2023, *ApJ*, 951, 106
- Britzen, S., Kudryavtseva, N. A., Witzel, A., et al. 2010, *A&A*, 511, A57
- Burke-Spolaor, S., Blecha, L., Bogdanović, T., et al. 2018, in *Astronomical Society of the Pacific Conference Series*, Vol. 517, *Science with a Next Generation Very Large Array*, ed. E. Murphy, 677
- Burke-Spolaor, S., Taylor, S. R., Charisi, M., et al. 2019, *A&A Rv*, 27, 5
- Caproni, A., & Abraham, Z. 2004a, *MNRAS*, 349, 1218
- . 2004b, *ApJ*, 602, 625
- Caproni, A., Abraham, Z., & Monteiro, H. 2013, *MNRAS*, 428, 280
- Caproni, A., Abraham, Z., Motter, J. C., & Monteiro, H. 2017, *ApJL*, 851, L39
- Casey-Clyde, J. A., Mingarelli, C. M. F., Greene, J. E., et al. 2022, *ApJ*, 924, 93
- Charisi, M., Bartos, I., Haiman, Z., et al. 2016, *MNRAS*, 463, 2145
- Charisi, M., Bartos, I., Haiman, Z., Price-Whelan, A. M., & Márka, S. 2015, *MNRAS*, 454, L21
- Charisi, M., Haiman, Z., Schiminovich, D., & D’Orazio, D. J. 2018, *MNRAS*, 476, 4617
- Charisi, M., Taylor, S. R., Runnoe, J., Bogdanovic, T., & Trump, J. R. 2022, *MNRAS*, 510, 5929
- Charisi, M., et al. 2023, in prep, doi:in prep
- Chen, X., Sesana, A., Madau, P., & Liu, F. K. 2011, *ApJ*, 729, 13
- Chen, Y.-C., Hwang, H.-C., Shen, Y., et al. 2022a, *ApJ*, 925, 162
- Chen, Y.-C., Liu, X., Liao, W.-T., et al. 2020, *MNRAS*, 499, 2245
- Chen, Y.-J., Zhai, S., Liu, J.-R., et al. 2022b, arXiv e-prints, arXiv:2206.11497
- CHIME/Pulsar Collaboration, Amiri, M., Bandura, K. M., et al. 2021, *ApJS*, 255, 5
- Christian, P., & Loeb, A. 2017, *MNRAS*, 469, 930
- Colpi, M. 2014, *SSR*, 183, 189
- Comerford, J. M., Schluns, K., Greene, J. E., & Cool, R. J. 2013, *ApJ*, 777, 64
- Corbin, V., & Cornish, N. J. 2010, arXiv e-prints, arXiv:1008.1782
- Corrales, L. R., Haiman, Z., & MacFadyen, A. 2010, *MNRAS*, 404, 947
- Coughlin, E. R., & Armitage, P. J. 2017, *MNRAS*, 471, L115
- . 2018, *MNRAS*, 474, 3857
- Coughlin, E. R., Armitage, P. J., Lodato, G., & Nixon, C. J. 2019, *SSR*, 215, 45

- Coughlin, E. R., Armitage, P. J., Nixon, C., & Begelman, M. C. 2017, *MNRAS*, 465, 3840
- Coughlin, E. R., Darbha, S., Kasen, D., & Quataert, E. 2018, *ApJL*, 863, L24
- Darbha, S., Coughlin, E. R., Kasen, D., & Quataert, E. 2018, *MNRAS*, 477, 4009
- d’Ascoli, S., Noble, S. C., Bowen, D. B., et al. 2018, *ApJ*, 865, 140
- Davelaar, J., & Haiman, Z. 2022a, *PRD*, 105, 103010
- . 2022b, *PhRvL*, 128, 191101
- Dayal, P., Rossi, E. M., Shiralilou, B., et al. 2019, *MNRAS*, 486, 2336
- De Rosa, A., Vignali, C., Bogdanović, T., et al. 2019, *NewAR*, 86, 101525
- Decarli, R., Dotti, M., Fumagalli, M., et al. 2013, *MNRAS*, 433, 1492
- Decarli, R., Dotti, M., Mazzucchelli, C., Montuori, C., & Volonteri, M. 2014, *MNRAS*, 445, 1558
- Decarli, R., Dotti, M., Montuori, C., Liimets, T., & Ederoclite, A. 2010, *ApJL*, 720, L93
- Dewdney, P. E., Hall, P. J., Schilizzi, R. T., & Lazio, T. J. L. W. 2009, *IEEE Proceedings*, 97, 1482
- Dexter, J., Lutz, D., Shimizu, T. T., et al. 2020, *ApJ*, 905, 33
- Dittmann, A. J., & Ryan, G. 2022, *MNRAS*, 513, 6158
- . 2023, *arXiv e-prints*, arXiv:2310.07758
- Djorgovski, S. G., et al. 2011, *ArXiv e-prints*, arXiv:1102.5004
- Doan, A., Eracleous, M., Runnoe, J. C., et al. 2020, *MNRAS*, 491, 1104
- D’Orazio, D. J., & Di Stefano, R. 2018, *MNRAS*, 474, 2975
- . 2020, *MNRAS*, 491, 1506
- D’Orazio, D. J., & Haiman, Z. 2017, *MNRAS*, 470, 1198
- D’Orazio, D. J., Haiman, Z., Duffell, P., Farris, B. D., & MacFadyen, A. I. 2015a, *MNRAS*, 452, 2540
- D’Orazio, D. J., Haiman, Z., Duffell, P., MacFadyen, A., & Farris, B. 2016, *Monthly Notices of the Royal Astronomical Society*, 459, 2379
- D’Orazio, D. J., Haiman, Z., & MacFadyen, A. 2013, *MNRAS*, 436, 2997
- D’Orazio, D. J., Haiman, Z., & Schiminovich, D. 2015b, *Nature*, 525, 351
- D’Orazio, D. J., & Loeb, A. 2018, *ApJ*, 863, 185
- . 2019, *PRD*, 100, 103016
- . 2020, *PRD*, 101, 083031
- . 2021, *PRD*, 104, 063015
- Dotti, M., Bonetti, M., D’Orazio, D. J., Haiman, Z., & Ho, L. C. 2022, *MNRAS*, 509, 212
- Dotti, M., Montuori, C., Decarli, R., et al. 2009, *MNRAS*, 398, L73
- Doğan, S., Nixon, C., King, A., & Price, D. J. 2015, *MNRAS*, 449, 1251
- Duffell, P. C., D’Orazio, D., Derdzinski, A., et al. 2020, *ApJ*, 901, 25
- Dunhill, A. C., Cuadra, J., & Dougados, C. 2015, *MNRAS*, 448, 3545
- E-ELT. 2023, <https://www.eso.org/sci/facilities/eelt/>, accessed: 2023-04-06
- Ebisuzaki, T., Makino, J., & Okumura, S. K. 1991, *Nature*, 354, 212
- EPTA Collaboration, InPTA Collaboration, Antoniadis, J., et al. 2023, *A&A*, 678, A50
- Eracleous, M., Boroson, T. A., Halpern, J. P., & Liu, J. 2012, *ApJS*, 201, 23
- Eracleous, M., & Halpern, J. P. 1994, *ApJS*, 90, 1
- . 2003, *ApJ*, 599, 886
- Eracleous, M., Halpern, J. P., M. Gilbert, A., Newman, J. A., & Filippenko, A. V. 1997, *ApJ*, 490, 216
- Eracleous, M., Lewis, K. T., & Flohic, H. M. L. G. 2009, *NewAR*, 53, 133
- Event Horizon Telescope Collaboration, Akiyama, K., Alberdi, A., et al. 2019, *ApJL*, 875, L1
- . 2022, *ApJL*, 930, L12
- Fabian, A. C., Iwasawa, K., Reynolds, C. S., & Young, A. J. 2000, *PASP*, 112, 1145
- Falxa, M., Babak, S., Baker, P. T., et al. 2023, *MNRAS*, arXiv:2303.10767
- Farris, B. D., Duffell, P., MacFadyen, A. I., & Haiman, Z. 2014, *ApJ*, 783, 134
- . 2015a, *MNRAS*, 447, L80
- . 2015b, *MNRAS*, 446, L36
- Fendt, C., & Yardimci, M. 2022, *ApJ*, 933, 71
- Foord, A., Liu, X., Gültekin, K., et al. 2022, *ApJ*, 927, 3
- Foord, A., Gültekin, K., Reynolds, M. T., et al. 2019, *ApJ*, 877, 17
- French, K. D., Arcavi, I., & Zabludoff, A. 2016, *ApJL*, 818, L21
- Fu, H., Zhang, Z.-Y., Assef, R. J., et al. 2011, *ApJL*, 740, L44
- Gardiner, E. C., Kelley, L. Z., Lemke, A.-M., & Mitridate, A. 2023, *arXiv e-prints*, arXiv:2309.07227
- Gardner, J. P., Mather, J. C., Clampin, M., et al. 2006, *SSR*, 123, 485
- Gaskell, C. M. 1983, in *Liege International Astrophysical Colloquia*, Vol. 24, *Liege International Astrophysical Colloquia*, ed. J.-P. Swings, 473–477
- Gaskell, C. M. 1996, *ApJL*, 464, L107
- Generozov, A., & Haiman, Z. 2014, *MNRAS*, 443, L64
- Gold, R., Paschalidis, V., Etienne, Z. B., Shapiro, S. L., & Pfeiffer, H. P. 2014a, *PRD*, 89, 064060
- Gold, R., Paschalidis, V., Ruiz, M., et al. 2014b, *PRD*, 90, 104030
- Goldstein, J. M., Sesana, A., Hologado, A. M., & Veitch, J. 2019, *MNRAS*, 485, 248
- Goldstein, J. M., Veitch, J., Sesana, A., & Vecchio, A. 2018, *MNRAS*, 477, 5447
- Gopal-Krishna, Biermann, P. L., & Wiita, P. J. 2003, *ApJL*, 594, L103

- Goulding, A. D., Pardo, K., Greene, J. E., et al. 2019, *ApJL*, 879, L21
- Goulding, A. D., Greene, J. E., Bezanson, R., et al. 2018, *PASJ*, 70, S37
- Gower, A. C., Gregory, P. C., Unruh, W. G., & Hutchings, J. B. 1982, *ApJ*, 262, 478
- Graham, M. J., Djorgovski, S. G., Stern, D., et al. 2015a, *Nature*, 518, 74
- . 2015b, *MNRAS*, 453, 1562
- Gravity+ Collaboration, Abuter, R., Alarcon, P., et al. 2022, *The Messenger*, 189, 17
- Grupe, D., Komossa, S., & Saxton, R. 2015, *ApJL*, 803, L28
- Gültekin, K., & Miller, J. M. 2012, *ApJ*, 761, 90
- Guo, H., Liu, X., Shen, Y., et al. 2019, *MNRAS*, 482, 3288
- Guo, H., Liu, X., Zafar, T., & Liao, W.-T. 2020, *MNRAS*, 492, 2910
- Gutiérrez, E. M., Combi, L., Noble, S. C., et al. 2022, *ApJ*, 928, 137
- Haiman, Z. 2017, *PRD*, 96, 023004
- Haiman, Z., Kocsis, B., & Menou, K. 2009, *ApJ*, 700, 1952
- Haiman, Z., Xin, C., Bogdanović, T., et al. 2023, *arXiv e-prints*, arXiv:2306.14990
- Hallinan, G., Ravi, V., Weinreb, S., et al. 2019, in *Bulletin of the American Astronomical Society*, Vol. 51, 255
- Halpern, J. P., & Filippenko, A. V. 1988, *Nature*, 331, 46
- Hayasaki, K., & Loeb, A. 2016, *Scientific Reports*, 6, 35629
- Hellings, R. W., & Downs, G. S. 1983, *ApJL*, 265, L39
- Hobbs, G. 2013, *Classical and Quantum Gravity*, 30, 224007
- Hobbs, G., Dai, S., Manchester, R. N., et al. 2019, *Research in Astronomy and Astrophysics*, 19, 020
- Hobbs, G., Archibald, A., Arzoumanian, Z., et al. 2010, *Classical and Quantum Gravity*, 27, 084013
- Hogg, D. W. 1999, *ArXiv Astrophysics e-prints*, astro-ph/9905116
- Holgado, A. M., Sesana, A., Sandrinelli, A., et al. 2018, *MNRAS*, 481, L74
- Hong, X. Y., Jiang, D. R., Gurvits, L. I., et al. 2004, *A&A*, 417, 887
- Hopkins, P. F., Richards, G. T., & Hernquist, L. 2007, *ApJ*, 654, 731
- Hu, B. X., D’Orazio, D. J., Haiman, Z., et al. 2020, *MNRAS*, 495, 4061
- Hwang, H.-C., Shen, Y., Zakamska, N., & Liu, X. 2020, *ApJ*, 888, 73
- Ingram, A., Motta, S. E., Aigrain, S., & Karastergiou, A. 2021, *MNRAS*, 503, 1703
- Ivezić, Ž., Kahn, S. M., Tyson, J. A., et al. 2019, *ApJ*, 873, 111
- Izquierdo-Villalba, D., Bonoli, S., Dotti, M., et al. 2020, *MNRAS*, 495, 4681
- Ji, X., Lu, Y., Ge, J., Yan, C., & Song, Z. 2021a, *ApJ*, 910, 101
- . 2021b, *ApJ*, 910, 101
- Joshi, B. C., Arumugasamy, P., Bagchi, M., et al. 2018, *Journal of Astrophysics and Astronomy*, 39, 51
- Ju, W., Greene, J. E., Rafikov, R. R., Bickerton, S. J., & Badenes, C. 2013, *ApJ*, 777, 44
- Jun, H. D., Stern, D., Graham, M. J., et al. 2015, *ApJL*, 814, L12
- Kaiser, A. R., & McWilliams, S. T. 2021, *Classical and Quantum Gravity*, 38, 055009
- Katz, M. L., Kelley, L. Z., Dosopoulou, F., et al. 2020, *MNRAS*, 491, 2301
- Kelley, L., Charisi, M., Burke-Spolaor, S., et al. 2019a, *BAAS*, 51, 490
- Kelley, L. Z. 2021, *MNRAS*, 500, 4065
- Kelley, L. Z., Blecha, L., & Hernquist, L. 2017a, *MNRAS*, 464, 3131
- Kelley, L. Z., Blecha, L., Hernquist, L., Sesana, A., & Taylor, S. R. 2017b, *MNRAS*, 471, 4508
- . 2018, *MNRAS*, 477, 964
- Kelley, L. Z., D’Orazio, D. J., & Di Stefano, R. 2021, *MNRAS*, 508, 2524
- Kelley, L. Z., Haiman, Z., Sesana, A., & Hernquist, L. 2019b, *MNRAS*, 485, 1579
- Kelly, B. J., Baker, J. G., Etienne, Z. B., Giacomazzo, B., & Schnittman, J. 2017, *PRD*, 96, 123003
- Kelly, B. J., Etienne, Z. B., Golomb, J., et al. 2021, *PRD*, 103, 063039
- Khan, A., Paschalidis, V., Ruiz, M., & Shapiro, S. L. 2018, *PRD*, 97, 044036
- Khan, F. M., Just, A., & Merritt, D. 2011, *ApJ*, 732, 89
- Kim, J.-Y., Krichbaum, T. P., Broderick, A. E., et al. 2020, *A&A*, 640, A69
- King, A., & Pounds, K. 2015, *ARA&A*, 53, 115
- Kollmeier, J. A., Zasowski, G., Rix, H.-W., et al. 2017, *arXiv e-prints*, arXiv:1711.03234
- Komberg, B. V. 1968, *Sov. Astron.*, 11, 727
- Komossa, S., Burwitz, V., Hasinger, G., et al. 2003, *ApJL*, 582, L15
- Komossa, S., Zhou, H., & Lu, H. 2008, *ApJL*, 678, L81
- Komossa, S., Grupe, D., Kraus, A., et al. 2021, *Universe*, 7, 261
- . 2023a, *MNRAS*, arXiv:2302.11646
- Komossa, S., Kraus, A., Grupe, D., et al. 2023b, *Astronomische Nachrichten*, 344, e20220126
- Kormendy, J., & Bender, R. 2009, *ApJL*, 691, L142
- Kormendy, J., & Ho, L. C. 2013, *ARA&A*, 51, 511
- Kormendy, J., & Richstone, D. 1995, *ARA&A*, 33, 581
- Koss, M., Mushotzky, R., Treister, E., et al. 2011, *ApJL*, 735, L42
- Koss, M., U, V., Hodges-Kluck, E., et al. 2019, *Astro2020: Decadal Survey on Astronomy and Astrophysics*, 2020, 504
- Koss, M. J., Treister, E., Kakkad, D., et al. 2023, *ApJL*, 942, L24
- Kozłowski, S., Kochanek, C. S., Udalski, A., et al. 2010, *ApJ*, 708, 927

- Kramer, M., & Champion, D. J. 2013, *Classical and Quantum Gravity*, 30, 224009
- Krauth, L. M., Davelaar, J., Haiman, Z., et al. 2023, *MNRAS*, arXiv:2304.02575
- Kulkarni, G., & Loeb, A. 2016, *MNRAS*, 456, 3964
- Kulkarni, G., Worseck, G., & Hennawi, J. F. 2019, *MNRAS*, 488, 1035
- Kun, E., Frey, S., & Gabányi, K. É. 2020, *MNRAS*, 496, 3336
- Kun, E., Frey, S., Gabányi, K. É., et al. 2015, *MNRAS*, 454, 1290
- Kun, E., Gabányi, K. É., Karouzos, M., Britzen, S., & Gergely, L. Á. 2014, *MNRAS*, 445, 1370
- Kurczynski, P., Johnson, M. D., Doeleman, S. S., et al. 2022, in *Society of Photo-Optical Instrumentation Engineers (SPIE) Conference Series*, Vol. 12180, *Space Telescopes and Instrumentation 2022: Optical, Infrared, and Millimeter Wave*, ed. L. E. Coyle, S. Matsuura, & M. D. Perrin, 121800M
- Lai, D. 2014, *MNRAS*, 440, 3532
- Lalakos, A., Gottlieb, O., Kaaz, N., et al. 2022, *ApJL*, 936, L5
- Lauer, T. R. 1985, *ApJ*, 292, 104
- Leahy, J. P., & Williams, A. G. 1984, *MNRAS*, 210, 929
- Lee, K. J. 2016, in *Astronomical Society of the Pacific Conference Series*, Vol. 502, *Frontiers in Radio Astronomy and FAST Early Sciences Symposium 2015*, ed. L. Qain & D. Li, 19
- Leighly, K. M., Terndrup, D. M., Gallagher, S. C., & Lucy, A. B. 2016, *ApJ*, 829, 4
- Leloudas, G., Fraser, M., Stone, N. C., et al. 2016, *Nature Astronomy*, 1, 0002
- Lezhnin, K., & Vasiliev, E. 2019, *MNRAS*, 484, 2851
- Liao, W.-T., Chen, Y.-C., Liu, X., et al. 2021, *MNRAS*, 500, 4025
- Lico, R., Jorstad, S. G., Marscher, A. P., et al. 2023, *Galaxies*, 11, 17
- Lippai, Z., Frei, Z., & Haiman, Z. 2008, *ApJL*, 676, L5
- Liska, M., Hesp, C., Tchekhovskoy, A., et al. 2018, *MNRAS*, 474, L81
- Liu, F. K., Li, S., & Chen, X. 2009, *ApJL*, 706, L133
- Liu, F. K., Li, S., & Komossa, S. 2014a, *ApJ*, 786, 103
- Liu, J., Eracleous, M., & Halpern, J. P. 2016, *ApJ*, 817, 42
- Liu, T., Cohen, T., McGrath, C., Demorest, P. B., & Vigeland, S. J. 2023, *ApJ*, 945, 78
- Liu, T., Gezari, S., & Miller, M. C. 2018a, *ApJL*, 859, L12
- Liu, T., & Vigeland, S. J. 2021, *ApJ*, 921, 178
- Liu, T., Gezari, S., Ayers, M., et al. 2019, *ApJ*, 884, 36
- Liu, T., Koss, M., Blecha, L., et al. 2020, *ApJ*, 896, 122
- Liu, X., Guo, H., Shen, Y., Greene, J. E., & Strauss, M. A. 2018b, *ApJ*, 862, 29
- Liu, X., Shen, Y., Bian, F., Loeb, A., & Tremaine, S. 2014b, *ApJ*, 789, 140
- Liu, X., Shen, Y., Strauss, M. A., & Greene, J. E. 2010, *ApJ*, 708, 427
- Lobanov, A. P., & Roland, J. 2005, *A&A*, 431, 831
- Lobanov, A. P., & Zensus, J. A. 2001, *Science*, 294, 128
- Luo, J., Chen, L.-S., Duan, H.-Z., et al. 2016, *Classical and Quantum Gravity*, 33, 035010
- Lynden-Bell, D. 1969, *Nature*, 223, 690
- MacFadyen, A. I., & Milosavljević, M. 2008, *ApJ*, 672, 83
- MacLeod, C. L., Ivezić, Ž., Kochanek, C. S., et al. 2010, *ApJ*, 721, 1014
- Mainzer, A., Bauer, J., Cutri, R. M., et al. 2014, *ApJ*, 792, 30
- Mangiagli, A., Caprini, C., Volonteri, M., et al. 2022, *PRD*, 106, 103017
- Mangiagli, A., Klein, A., Bonetti, M., et al. 2020, *PRD*, 102, 084056
- Marchesi, S., Gilli, R., Lanzuisi, G., et al. 2020, *A&A*, 642, A184
- Margalit, B., Metzger, B. D., Berger, E., et al. 2018, *MNRAS*, 481, 2407
- Martin, D. C., Fanson, J., Schiminovich, D., et al. 2005, *ApJL*, 619, L1
- Martini, P. 2004, in *Coevolution of Black Holes and Galaxies*, ed. L. C. Ho, 169
- Martizzi, D., Teyssier, R., & Moore, B. 2013, *MNRAS*, 432, 1947
- McGrath, C., & Creighton, J. 2021, *MNRAS*, 505, 4531
- McGrath, C., D’Orazio, D. J., & Creighton, J. 2022, *MNRAS*, 517, 1242
- McGurk, R. C., Max, C. E., Medling, A. M., Shields, G. A., & Comerford, J. M. 2015, *ApJ*, 811, 14
- McKernan, B., Ford, K. E. S., Kocsis, B., & Haiman, Z. 2013, *MNRAS*, 432, 1468
- McLaughlin, M. A. 2013, *Classical and Quantum Gravity*, 30, 224008
- Meliani, Z., Mizuno, Y., Olivares, H., et al. 2017, *A&A*, 598, A38
- Merritt, D. 2006, *ApJ*, 648, 976
- Merritt, D., & Ekers, R. D. 2002, *Science*, 297, 1310
- Merritt, D., & Milosavljević, M. 2005, *Living Reviews in Relativity*, 8
- Merritt, D., & Poon, M. Y. 2004, *ApJ*, 606, 788
- Mignon-Risse, R., Varniere, P., & Casse, F. 2023, *MNRAS*, arXiv:2301.06566
- Millon, M., Dalang, C., Lemon, C., et al. 2022, *A&A*, 668, A77
- Milosavljević, M., & Merritt, D. 2003, *ApJ*, 596, 860
- Milosavljević, M., Merritt, D., Rest, A., & van den Bosch, F. C. 2002, *MNRAS*, 331, L51
- Mingarelli, C. M. F., Sidery, T., Mandel, I., & Vecchio, A. 2013, *PRD*, 88, 062005
- Mingarelli, C. M. F., Lazio, T. J. W., Sesana, A., et al. 2017, *Nature Astronomy*, 1, 886
- Moesta, P., Alic, D., Rezzolla, L., Zanotti, O., & Palenzuela, C. 2012, *ApJL*, 749, L32
- Mohan, P., An, T., Frey, S., et al. 2016, *MNRAS*, 463, 1812
- Moody, M. S. L., Shi, J.-M., & Stone, J. M. 2019, *ApJ*, 875, 66

- Moore, C. J., Cole, R. H., & Berry, C. P. L. 2015, *Classical and Quantum Gravity*, 32, 015014
- Moore, C. J., Mihaylov, D. P., Lasenby, A., & Gilmore, G. 2017, *PhRvL*, 119, 261102
- Muñoz, D. J., Miranda, R., & Lai, D. 2019, *ApJ*, 871, 84
- Müller-Sánchez, F., Comerford, J. M., Nevin, R., et al. 2015, *ApJ*, 813, 103
- Muñoz, D. J., & Lai, D. 2016, *arXiv.org*, arXiv:1604.00004
- Nair, S., Jin, C., & Garrett, M. A. 2005, *MNRAS*, 362, 1157
- Nandra, K., Barret, D., Barcons, X., et al. 2013, *arXiv e-prints*, arXiv:1306.2307
- Narayan, R., & Yi, I. 1995, *ApJ*, 452, 710
- Nevin, R., Comerford, J., Müller-Sánchez, F., Barrows, R., & Cooper, M. 2016, *ApJ*, 832, 67
- Nguyen, K., & Bogdanović, T. 2016, *ApJ*, 828, 68
- Nguyen, K., Bogdanović, T., Runnoe, J. C., et al. 2019, *ApJ*, 870, 16
- . 2020, *ApJ*, 894, 105
- Noble, S. C., Krolik, J. H., Campanelli, M., et al. 2021, *ApJ*, 922, 175
- Noble, S. C., Krolik, J. H., & Hawley, J. F. 2009, *ApJ*, 692, 411
- Noble, S. C., et al. 2012, *ApJ*, 755, 51
- Ogiya, G., Hahn, O., Mingarelli, C. M. F., & Volonteri, M. 2020, *MNRAS*, 493, 3676
- O'Neill, S., Kiehlmann, S., Readhead, A. C. S., et al. 2022, *ApJL*, 926, L35
- Osterbrock, D. E., & Mathews, W. G. 1986, *ARA&A*, 24, 171
- Owen, F. N., O'Dea, C. P., Inoue, M., & Eilek, J. A. 1985, *ApJL*, 294, L85
- Palenzuela, C., Lehner, L., & Liebling, S. L. 2010, *Science*, 329, 927
- Pardo, K., Chang, T.-C., Doré, O., & Wang, Y. 2023, *arXiv e-prints*, arXiv:2306.14968
- Perets, H. B., Hopman, C., & Alexander, T. 2007, *ApJ*, 656, 709
- Peterson, B. M. 2014, *SSR*, 183, 253
- Pflueger, B. J., Nguyen, K., Bogdanović, T., et al. 2018, *ApJ*, 861, 59
- Piro, L., Colpi, M., Aird, J., et al. 2023, *MNRAS*, 521, 2577
- Popović, L. Č., Jovanović, P., Stalevski, M., et al. 2012, *A&A*, 538, A107
- Predehl, P., Andrichke, R., Arefiev, V., et al. 2021, *A&A*, 647, A1
- Preto, M., Berentzen, I., Berczik, P., & Spurzem, R. 2011, *ApJL*, 732, L26
- Qian, S. J., Britzen, S., Krichbaum, T. P., & Witzel, A. 2019, *A&A*, 621, A11
- . 2021, *A&A*, 653, A7
- Qian, S. J., Britzen, S., Witzel, A., Krichbaum, T. P., & Gan, H. Q. 2017, *A&A*, 604, A90
- Qian, S. J., Britzen, S., Witzel, A., Krichbaum, T. P., & Kun, E. 2018, *A&A*, 615, A123
- Qian, S.-J., Witzel, A., Zensus, J. A., et al. 2009, *Research in Astronomy and Astrophysics*, 9, 137
- Ragusa, E., Alexander, R., Calcino, J., Hirsh, K., & Price, D. J. 2020, *MNRAS*, 499, 3362
- Ragusa, E., Lodato, G., & Price, D. J. 2016, *MNRAS*, 460, 1243
- Rantala, A., Johansson, P. H., Naab, T., Thomas, J., & Frigo, M. 2018, *ApJ*, 864, 113
- Ravi, V., Wyithe, J. S. B., Hobbs, G., et al. 2012, *ApJ*, 761, 84
- Reardon, D. J., Zic, A., Shannon, R. M., et al. 2023, *ApJL*, 951, L6
- Rees, M. J. 1978, *Nature*, 275, 516
- Ren, G.-W., Ding, N., Zhang, X., et al. 2021, *MNRAS*, 506, 3791
- Ricarte, A., & Natarajan, P. 2018, *MNRAS*, 481, 3278
- Ricarte, A., Natarajan, P., Dai, L., & Coppi, P. 2016, *MNRAS*, 458, 1712
- Rieger, F. M. 2004, *ApJL*, 615, L5
- Robinson, I., Schild, A., & Schucking, E. L., eds. 1965, *Quasi-stellar sources and gravitational collapse*
- Rodriguez, C., Taylor, G. B., Zavala, R. T., et al. 2006, *ApJ*, 646, 49
- Roedig, C., Krolik, J. H., & Miller, M. C. 2014, *ApJ*, 785, 115
- Roland, J., Britzen, S., Kudryavtseva, N. A., Witzel, A., & Karouzos, M. 2008, *A&A*, 483, 125
- Roland, J., Gattano, C., Lambert, S. B., & Taris, F. 2020, *A&A*, 634, A101
- Romero, G. E., Chajet, L., Abraham, Z., & Fan, J. H. 2000, *A&A*, 360, 57
- Roming, P. W. A., Kennedy, T. E., Mason, K. O., et al. 2005, *SSR*, 120, 95
- Roos, N. 1988, *ApJ*, 334, 95
- Roos, N., Kaastra, J. S., & Hummel, C. A. 1993, *ApJ*, 409, 130
- Rosado, P. A., Sesana, A., & Gair, J. 2015, *MNRAS*, 451, 2417
- Rossi, E. M., Lodato, G., Armitage, P. J., Pringle, J. E., & King, A. R. 2010, *MNRAS*, 401, 2021
- Runnoe, J. C., Eracleous, M., Mathes, G., et al. 2015, *ApJS*, 221, 7
- Runnoe, J. C., Eracleous, M., Pennell, A., et al. 2017, *MNRAS*, 468, 1683
- Ryan, G., & MacFadyen, A. 2017, *ApJ*, 835, 199
- Ryu, T., Perna, R., Haiman, Z., Ostriker, J. P., & Stone, N. C. 2018, *MNRAS*, 473, 3410
- Saade, M. L., Stern, D., Brightman, M., et al. 2020, *ApJ*, 900, 148
- Saade, M. L., Brightman, M., Stern, D., et al. 2023, *arXiv e-prints*, arXiv:2304.06144
- Salcido, J., Bower, R. G., Theuns, T., et al. 2016, *MNRAS*, 463, 870
- Sandrinelli, A., Covino, S., Treves, A., et al. 2018, *A&A*, 615, A118
- Sato-Polito, G., & Kamionkowski, M. 2023, *arXiv e-prints*, arXiv:2305.05690
- Schmidt, M. 1963, *Nature*, 197, 1040
- Serafinelli, R., Severgnini, P., Braito, V., et al. 2020, *ApJ*, 902, 10

- Sesana, A., Haardt, F., Madau, P., & Volonteri, M. 2005, *ApJ*, 623, 23
- Sesana, A., Haiman, Z., Kocsis, B., & Kelley, L. Z. 2018, *ApJ*, 856, 42
- Sesana, A., Roedig, C., Reynolds, M. T., & Dotti, M. 2012, *MNRAS*, 420, 860
- Shakura, N. I., & Sunyaev, R. A. 1973, *A&A*, 24, 337
- Shankar, F., Weinberg, D. H., & Miralda-Escudé, J. 2013, *MNRAS*, 428, 421
- Shen, Y., Greene, J. E., Strauss, M. A., Richards, G. T., & Schneider, D. P. 2008, *ApJ*, 680, 169
- Shen, Y., Hwang, H.-C., Zakamska, N., & Liu, X. 2019, *ApJL*, 885, L4
- Shen, Y., Liu, X., Loeb, A., & Tremaine, S. 2013, *ApJ*, 775, 49
- Shen, Y., & Loeb, A. 2010, *ApJ*, 725, 249
- Shen, Y., Greene, J. E., Ho, L. C., et al. 2015, *ApJ*, 805, 96
- Shi, J.-M., & Krolik, J. H. 2015, *ApJ*, 807, 131
- Shi, J.-M., Krolik, J. H., Lubow, S. H., & Hawley, J. F. 2012, *ApJ*, 749, 118
- Shields, G. A., Rosario, D. J., Smith, K. L., et al. 2009, *ApJ*, 707, 936
- Shu, X., Zhang, W., Li, S., et al. 2020, *Nature Communications*, 11, 5876
- Sirko, E., & Goodman, J. 2003, *MNRAS*, 341, 501
- Siwek, M., Weinberger, R., Muñoz, D. J., & Hernquist, L. 2023, *MNRAS*, 518, 5059
- Smallwood, J. L., Lubow, S. H., & Martin, R. G. 2022, *MNRAS*, 514, 1249
- Song, Z., Ge, J., Lu, Y., Yan, C., & Ji, X. 2021, *A&A*, 645, A15
- Soyuer, D., Zwick, L., D’Orazio, D. J., & Saha, P. 2021, *MNRAS*, 503, L73
- Stappers, B. W., Keane, E. F., Kramer, M., Possenti, A., & Stairs, I. H. 2018, *Philosophical Transactions of the Royal Society of London Series A*, 376, 20170293
- Stemo, A., Comerford, J. M., Barrows, R. S., et al. 2020, *ApJ*, 888, 78
- Stirling, A. M., Cawthorne, T. V., Stevens, J. A., et al. 2003, *MNRAS*, 341, 405
- Stockton, A., & Farnham, T. 1991, *ApJ*, 371, 525
- Sudarshan, P., Penzlin, A. B. T., Ziampras, A., Kley, W., & Nelson, R. P. 2022, *A&A*, 664, A157
- Tanaka, T., Menou, K., & Haiman, Z. 2012, *MNRAS*, 420, 705
- Tang, Y., Haiman, Z., & MacFadyen, A. 2018, *MNRAS*, 476, 2249
- Taylor, S., Burke-Spolaor, S., Baker, P. T., et al. 2019, *BAAS*, 51, 336
- Taylor, S. R. 2021, *arXiv e-prints*, arXiv:2105.13270
- Taylor, S. R., van Haasteren, R., & Sesana, A. 2020, *PRD*, 102, 084039
- The International Pulsar Timing Array Collaboration, Agazie, G., Antoniadis, J., et al. 2023, *arXiv e-prints*, arXiv:2309.00693
- The LIGO Scientific Collaboration, the Virgo Collaboration, the KAGRA Collaboration, et al. 2021, *arXiv e-prints*, arXiv:2111.03606
- Thomas, J., Ma, C.-P., McConnell, N. J., et al. 2016, *Nature*, 532, 340
- Thompson, T. A., Quataert, E., & Murray, N. 2005, *ApJ*, 630, 167
- Thorne, K. S., & Braginskii, V. B. 1976, *ApJL*, 204, L1
- Tiede, C., Zrake, J., MacFadyen, A., & Haiman, Z. 2020, *ApJ*, 900, 43
- . 2022, *ApJ*, 932, 24
- Tofflemire, B. M., Mathieu, R. D., Herczeg, G. J., Akeson, R. L., & Ciardi, D. R. 2017, *ApJL*, 842, L12
- Tremmel, M., Governato, F., Volonteri, M., Quinn, T. R., & Pontzen, A. 2018, *MNRAS*, 475, 4967
- Tsai, C.-W., Jarrett, T. H., Stern, D., et al. 2013, *ApJ*, 779, 41
- Tsalmantza, P., Decarli, R., Dotti, M., & Hogg, D. W. 2011, *ApJ*, 738, 20
- Valtonen, M., & Pihajoki, P. 2013, *A&A*, 557, A28
- Valtonen, M. J., Lehto, H. J., Nilsson, K., et al. 2008, *Nature*, 452, 851
- Valtonen, M. J., Zola, S., Gopakumar, A., et al. 2023, *MNRAS*, 521, 6143
- Vaughan, S., Uttley, P., Markowitz, A. G., et al. 2016, *MNRAS*, 461, 3145
- Villata, M., & Raiteri, C. M. 1999, *A&A*, 347, 30
- Volonteri, M., Pfister, H., Beckmann, R. S., et al. 2020, *MNRAS*, 498, 2219
- Wang, H.-Y., Bai, X.-N., & Lai, D. 2023a, *ApJ*, 943, 175
- Wang, H.-Y., Bai, X.-N., Lai, D., & Lin, D. N. C. 2023b, *MNRAS*, 526, 3570
- Wang, J.-M., Chen, Y.-M., Hu, C., et al. 2009, *ApJL*, 705, L76
- Wang, J.-M., & Li, Y.-R. 2020, *Research in Astronomy and Astrophysics*, 20, 160
- Wang, J.-M., Songsheng, Y.-Y., Li, Y.-R., & Du, P. 2023c, *MNRAS*, 518, 3397
- Wang, L., Greene, J. E., Ju, W., et al. 2017, *ApJ*, 834, 129
- Wang, L.-F., Shao, Y., Zhang, J.-F., & Zhang, X. 2022a, *arXiv e-prints*, arXiv:2201.00607
- Wang, Y., Zhai, Z., Alavi, A., et al. 2022b, *ApJ*, 928, 1
- Westernacher-Schneider, J. R., Zrake, J., MacFadyen, A., & Haiman, Z. 2022, *PRD*, 106, 103010
- Will, C. M., Naoz, S., Hees, A., et al. 2023, *arXiv e-prints*, arXiv:2307.16646
- Witt, C. A., Charisi, M., Taylor, S. R., & Burke-Spolaor, S. 2022, *ApJ*, 936, 89
- Wrobel, J. M., & Lazio, T. J. W. 2021, *arXiv e-prints*, arXiv:2108.07341
- . 2022, *ApJ*, 931, 12
- Xin, C., Charisi, M., Haiman, Z., & Schiminovich, D. 2020a, *MNRAS*, 495, 1403

- Xin, C., Charisi, M., Haiman, Z., et al. 2020b, MNRAS, 496, 1683
- Xin, C., & Haiman, Z. 2021, MNRAS, 506, 2408
- Xu, H., Chen, S., Guo, Y., et al. 2023, Research in Astronomy and Astrophysics, 23, 075024
- Yan, C.-S., Lu, Y., Dai, X., & Yu, Q. 2015, ApJ, 809, 117
- Yang, X., Joshi, R., Gopal-Krishna, et al. 2019, ApJS, 245, 17
- Yu, Q. 2002, MNRAS, 331, 935
- Zevin, M., Bavera, S. S., Berry, C. P. L., et al. 2021, ApJ, 910, 152
- Zhang, W., Basu-Zych, A., Bautz, M., et al. 2022, in AAS/High Energy Astrophysics Division, Vol. 54, AAS/High Energy Astrophysics Division, 108.45
- Zhao, W., Hong, X. Y., An, T., et al. 2011, A&A, 529, A113
- Zheng, Z.-Y., Butler, N. R., Shen, Y., et al. 2016, ApJ, 827, 56
- Zhou, J., Wang, Z., Chen, L., et al. 2018, Nature Communications, 9, 4599
- Zhu, X.-J., & Thrane, E. 2020, ApJ, 900, 117
- Zrake, J., Tiede, C., MacFadyen, A., & Haiman, Z. 2021, ApJL, 909, L13